

Formation conditions of leucogranite dykes and aplite-pegmatite dykes in the eastern Mt. Capanne plutonic complex (Elba, Italy): fluid inclusion studies in quartz, tourmaline, andalusite and plagioclase

Ronald J. Bakker & Sebastian E. Schilli

Mineralogy and Petrology

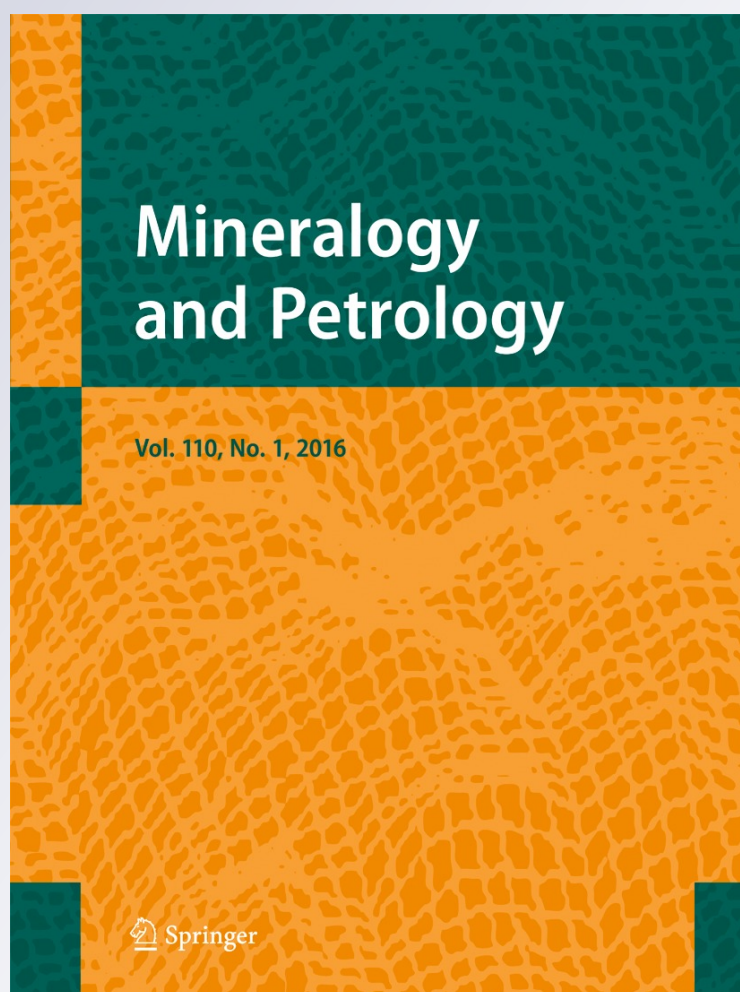
ISSN 0930-0708

Volume 110

Number 1

Miner Petrol (2016) 110:43-63

DOI 10.1007/s00710-015-0417-z



Your article is protected by copyright and all rights are held exclusively by Springer-Verlag Wien. This e-offprint is for personal use only and shall not be self-archived in electronic repositories. If you wish to self-archive your article, please use the accepted manuscript version for posting on your own website. You may further deposit the accepted manuscript version in any repository, provided it is only made publicly available 12 months after official publication or later and provided acknowledgement is given to the original source of publication and a link is inserted to the published article on Springer's website. The link must be accompanied by the following text: "The final publication is available at link.springer.com".

Formation conditions of leucogranite dykes and aplite-pegmatite dykes in the eastern Mt. Capanne plutonic complex (Elba, Italy): fluid inclusion studies in quartz, tourmaline, andalusite and plagioclase

Ronald J. Bakker¹ · Sebastian E. Schilli¹

Received: 24 May 2015 / Accepted: 25 November 2015 / Published online: 23 December 2015
© Springer-Verlag Wien 2015

Abstract Leucogranite and aplite-pegmatite dykes are associated with the Mt. Capanne pluton (Elba) and partly occur in the thermally metamorphosed host rock (serpentinites). Crystallization conditions of these dykes in the late magmatic-hydrothermal stage are estimated from fluid inclusion studies and mineralogical characterisation, obtained from detailed microthermometry, Raman spectroscopy, and electron microprobe analyses. Fluid inclusion assemblages are analysed in andalusite, quartz, and plagioclase from the leucogranite dykes, and in tourmaline and quartz from the aplite-pegmatite dykes. The fluid inclusion assemblages record multiple pulses of low salinity H₂O-rich magmatic and reduced metamorphic fluid stages. Magmatic fluids are characterized by the presence of minor amounts of CO₂ and H₃BO₃, whereas the metamorphic fluids contain CH₄ and H₂. The highly reduced conditions are also inferred from the presence of native arsenic in some fluid inclusions. Several fluid inclusion assemblages reveal fluid compositions that must have resulted from mixing of both fluid sources. In leucogranite dykes, magmatic andalusite contains a low-density magmatic CO₂-rich gas mixture with minor amounts of CH₄ and H₂. Accidentally trapped crystals (mica) and step-daughters (quartz and diaspore) are detected in some inclusions in andalusite. The first generation of inclusions in quartz that crystallized after andalusite contains

a highly reduced H₂O-H₂ mixture and micas. The second type of inclusions in quartz from the leucogranite is similar to the primary inclusion assemblage in tourmaline from the aplite-pegmatite, and contains up to 4.2 mass% H₃BO₃, present as a sassolite daughter crystal or dissolved ions, in addition to a CO₂-CH₄ gas mixture, with traces of H₂, N₂, H₂S, and C₂H₆. H₂O is the main component of all these fluids ($x=0.91$ to 0.96) with maximally 7 mass% NaCl. Some accidentally trapped arsenolite and native arsenic are also detected. These fluids were trapped in the leucogranite at about 670–720 °C and 270–310 MPa, which is determined by combining isochore reconstruction, limits of the stability field of magmatic andalusite, and the water-saturated granite solidus. Trapping conditions of the aplite-pegmatites are at similar temperatures and slightly lower pressures, at 230–270 MPa. The third type of fluid inclusion assemblages in quartz in the leucogranite represents a continuously trapping event down to 200 °C and 50 MPa, whereas the aplite pegmatite records a distinct trapping event of inclusions in quartz at about 250–300 °C and 50–100 MPa.

Introduction

The Monte Capanne pluton in western Isola d'Elba (Italy) is a monzogranite belonging to the Neogene-Quaternary Tuscan Magmatic Province of central Italy (e.g., Innocenti et al. 1992; Dini et al. 2002 and reference therein). Fluid inclusion studies from igneous rock and associated metamorphic rock to understand rock-forming conditions in and around the Monte Capanne complex are rare (Ruggieri and Lattanzi 1992; Rossetti and Tecce 2008). Analyses of some individual fluid inclusions from unspecified Elba pegmatites without further petrographical characterizations were mentioned by Peretyazhko et al. (2000) and Thomas (2002). The late magmatic-hydrothermal stage of these intrusive rocks is

Editorial handling: P. S. Garofalo

Electronic supplementary material The online version of this article (doi:10.1007/s00710-015-0417-z) contains supplementary material, which is available to authorized users.

✉ Ronald J. Bakker
bakker@unileoben.ac.at

¹ Department of Applied Geosciences and Geophysics, Montanuniversitaet Leoben, Leoben, Austria

associated with abundant fluid sources, of which the remnants are present in numerous fluid inclusion assemblages in the Monte Capanne and Porto Azzuro monzogranite, associated leucogranite and aplite-pegmatite dykes and sills, and monzodiorite of the Orano porphyry (Schilli 2015). The present study reveals detailed analyses of fluid inclusions assemblages in tourmaline and quartz from aplite-pegmatite dykes, in comparison to assemblages in andalusite, plagioclase and quartz from leucogranite dykes in a serpentinite host-rock from the metamorphosed ophiolitic-sedimentary tectonic Complex IV in contact to the eastern part of the Monte Capanne pluton (e.g., Benvenuti et al. 2001; Bortolotti et al. 2001). The mineralogy and fluid chemistry of the samples are used in this study to characterize the nature of the environment of formation of these igneous bodies.

Geology of sample area

The Monte Capanne pluton is a voluminous monzogranite that is relatively homogeneous in chemistry and slightly peraluminous (e.g., Dini et al. 2002). Westerman et al. (2004a) and Dini et al. (2004) suggested that the pluton was hybridized from mantle and crustally derived magma, based on ample geochemical and petrographical data. The age of the emplacement is about 6.9 Ma (Innocenti et al. 1992; Dini et al. 2002). The pluton was emplaced in the deepest levels of a stack of nappes of lower Ligurian complexes, i.e., tectonic Complexes IV (contact-metamorphosed ophiolitic-sedimentary unit) and V (unmetamorphosed flysch) in western Elba. The conditions of emplacement were inferred from 1. erosion reconstructions, resulting in an approximate depth of 4.5 km (Westerman et al. 2004b), and 2. metamorphic reactions in the thermally metamorphosed host rock, illustrating an undefined excess to 600 °C at 100–200 MPa (Dini et al. 2002). The poorly constrained andalusite-sillimanite transition (Kerrick 1990), talc/forsterite dehydration to anthophyllite, and the breakdown of muscovite and quartz were used to characterize emplacement conditions. In the eastern part of the Monte Capanne pluton most of the rocks in Complex IV are serpentinites, which are affected by thermal metamorphism of the intrusion.

The Monte Capanne pluton is associated with numerous leucogranite dykes and aplite-pegmatite dykes and veins (e.g., Pezzotta 2000; Dini et al. 2002). They occur mainly in the pluton and its thermometamorphic aureole close to the pluton's contact. The leucogranite dykes have a thickness up to 10 m and dip steeply towards ESE in the eastern part of the pluton. The aplite-pegmatite dykes are only 0.1 to 2 m thick, locally zoned, and crosscutting the leucogranite dykes (e.g., Ruggieri and Lattanzi 1992; Pezzotta 2000). The leucogranite dykes are peraluminous and have the highest SiO₂ and the lowest Al₂O₃ content compared to other igneous rock from

Elba (Dini et al. 2002), and they are interpreted as a series of fractionation products from a magma having characteristics similar to those of the San Piero facies of the Monte Capanne pluton. Tourmaline bearing aplite-pegmatite dykes are mainly known for Li-bearing minerals (e.g., Pezzotta 2000), and detailed analyses of mineral compositions such as foitite-elbaite (e.g., Aurisicchio et al. 1999) and beryl (e.g., Aurisicchio et al. 2012).

Analytical methods

Microthermometry measurements were carried out with a LINKAM MDS 600 and LINKAM THMSG 600 heating–freezing stage. Calibration was done by using synthetic fluid inclusions with melting of CO₂ at –56.6 °C (triple point), melting of water at 0.0 °C (triple point) and the critical homogenization temperature of water at 374.0 °C. The instrument resolution of both stages is 0.1 °C, and the standard deviation in each measurement is ±0.2 °C in the range of –50 to +50 °C, and increases towards higher temperatures, up to ±0.5 °C at 400 °C.

The shape of fluid inclusions was described by using the terminology of Bakker and Diamond (2006) that defines elongation and regularity. The volume fraction of the vapour is set equal to the area fraction observed in two-dimensional images, which may introduce a specific uncertainty. Bakker and Diamond (2006) have illustrated that this uncertainty is insignificant for regular shaped inclusions, using a spindle stage. Doppler et al. (2013) compared area fractions of the vapour phase with calculated fractions from homogenization temperatures of pure H₂O fluid inclusions, and concluded that the observed area fractions without the use of a spindle stage can be up to 15 % smaller.

The units and symbols of quantities such as fractions that are used in this study are strictly according to SI (Bakker 2011). The use of “weight fraction” is omitted because it is an erroneous label for mass fraction (*w*). Amount fraction (*x*) is used in this study to quantify the ratio of amount of substances, which is also known as “mole fraction”. A unit name (mole) should not be confused with a physical quantity.

Raman spectroscopic measurements were used to detect fluid components, entrapped minerals, and phase assemblage determination at low temperatures in single inclusions (down to –180 °C; see also Bakker 2004; Baumgartner and Bakker 2010). Raman spectroscopy was performed with a LABRAM (ISA Jobin–Yvon) confocal spectrometer using a frequency-doubled 100-mW Nd-YAG laser with an excitation wavelength of $\lambda = 532.068$ nm. The laser power at the sample surface is about 1 to 2 mW. An edge-filter (532 nm) was used to suppress Rayleigh scattering and anti-Stokes scattering, blocking relative wavenumbers below 80 cm^{–1}. All measurements were performed with an LMPlanFI 100x/0.80

(Olympus) objective lens. Wavenumber measurements have a precision of 1.62 cm^{-1} at low $\Delta\nu$ (Raman shift around 0 cm^{-1}) and 1.1 cm^{-1} at high $\Delta\nu$ (around 3000 cm^{-1}). The area of specific Raman peaks (intensity $\times \text{cm}^{-1}$) were used to calculate gas compositions according to Placzek's polarizability theory (e.g., Burke 2001).

Electron microprobe analyses of tourmaline, andalusite, and rutile were completed with the Superprobe JEOL JXA 8200 in the ESML (Eugen F. Stumpfl Microprobe Laboratory) of the Montanuniversitaet Leoben. The elements B, F, Na, Mg, Al, Si, K, Ca, Ti, Mn, and Fe were analysed in tourmaline with 20 keV and 10 nA, using counting times as short as 10 and 20 s for background and peak, respectively. The elements Al, Si, Fe, Mg, Mn, Ti, Na, Ca, and K were analysed in andalusite, whereas the elements Ti, Al, Fe, Mn, Cr, Sn, W, Nb, Ta, and Zr were analysed in rutile. Details on detection limits, standards, and analyzing crystals are given in Schilli (2015).

The software package *FLUIDS* (Bakker 2003) and *CLATHRATES* (Bakker 1997), and newly developed programs (<http://fluids.unileoben.ac.at>) were used to calculate fluid properties of fluid inclusions from microthermometry, Raman spectroscopy (gas mixtures) and optical properties. Program *ICE* from the package *CLATHRATES* (Bakker 1997) was used to calculate bulk fluid properties from $T_m(\text{ice})$, $T_m(\text{clathrate})$, gas-mixture composition, and vapour volume fraction estimations. In absence of exact knowledge of $T_m(\text{clathrate})$ but with indications of its similarity to $T_m(\text{ice})$, the program *ICE* was used to estimate bulk fluid properties at Q_1 clathrate dissolution conditions (see Bakker et al. 1996; Bakker 1998). Within this program, the properties of low-density gas mixtures are calculated with the equation of state from Peng and Robinson (1976), and the aqueous liquid solution is approximately characterized with Duan et al. (1992). Furthermore, the osmotic coefficient (Pitzer 1991) of dissolved ions is used to calculate the activity of H_2O in the aqueous solution, and to calculate the salinity in terms of NaCl concentrations. Homogenization temperatures and isochores of pure H_2O and mixed H_2O -NaCl fluid systems were analysed with the program *Loner HGK* (equation of state Haar et al. 1984), and with the program *AqSo DH* (equation of state Driesner and Heinrich 2007; Driesner 2007), respectively. These fluid systems can be used as an approximation of natural fluid inclusions that contain less than 5 amount % of gases and salts. The programs *Loner AP* (equation of state Anderko and Pitzer 1993; Duan et al. 1995, 2003) and *Loner B* (Bakker 1999) were mainly used to calculate isochores in complex H_2O - CO_2 - CH_4 -NaCl fluid systems. These equations of state do not provide accurate estimations of bulk fluid densities from measured homogenization temperatures in the present study. The accuracy of isochore estimates is obtained from comparison of the pure end-member fluids with modified Helmholtz equations of

state (e.g., Haar et al. 1984 for pure H_2O). The program *AqSo WHS* (Bakker 2012) was used to calculate equivalent mass fractions of NaCl in binary H_2O -NaCl systems.

Location and mineralogy of samples

Samples from two dykes (67E and 85A) were collected in serpentinites close to the contact with the Monte Capanne pluton near San Piero in Campo and Sant'Ilario. Sample 67E was collected along the hiking trail between Grotta d'Oggi and San Piero in Campo (N $42^\circ 45' 15.4''$, E $010^\circ 12' 58.6$). This cordierite-bearing leucogranite dyke has an orientation of 070/70. Sample 85A is from a 50 cm thick tourmaline-bearing aplite-pegmatite dyke along the hiking trail from La Pila to C. Mastaglino (N $42^\circ 46' 04.2''$, E $010^\circ 13' 25.9''$). Abundant secondary nodular magnesite aggregates were observed in the neighbouring serpentinites.

Locally, sample 67E has pinkish colours due to abundant presence of andalusite, and several greenish spots (cordierite), in addition to the main components quartz and plagioclase (mainly albite-rich). Despite the strong peraluminous character of the leucogranite dykes, andalusite has only been regarded as an insignificant accessory in previous studies (e.g., Pezzotta 2000). The andalusite is zoned with a pink core, due to relative enrichment of Fe (up to 2.7 mass% FeO, see Electronic Appendix A) and colourless rims. The cordierite is partly altered (pinitization), and contains yellow pleochroic halos. The accessory minerals rutile, xenotime, apatite, monazite, and zircon with grain sizes between 1 and $10 \mu\text{m}$ have been mainly detected by Raman spectroscopy. Xenotime and rutile have not been reported in previous studies of leucogranite dykes. The rutile is extremely enriched in Fe, Nb, Sn, and Ta, up to 11.5, 7.0, 4.3, and 3.9 mass% of the oxides, respectively (see Electronic Appendix B).

Sample 85A is coarse grained, mainly composed of quartz, plagioclase (albite-rich) and tourmaline crystals up to 5 cm in length. The tourmaline is strongly zoned with a bluish-green core and darker brownish-green rim. The core is a foitic tourmaline, whereas the rims are schorlitic tourmalines (see Electronic Appendix C), with abundant vacancies in the X-position for both core and rim (X-site vacancy tourmaline, classification of Hawthorne and Henry 1999; Clark 2007). The rims are relatively enriched in FeO, TiO_2 and Na_2O , whereas they are depleted in Al_2O_3 at the Y-position. Compared to tourmaline analyses in similar rocks described by Aurisicchio et al. (1999), our results illustrate enrichment in Na_2O , CaO, TiO_2 and MgO, and depletion in MnO and FeO, which may be caused by the compositional variation in well-defined growth-zones in tourmaline, or by strong interaction of the intrusive aplite-pegmatite dykes with host-rock (serpentinites) during tourmaline growth.

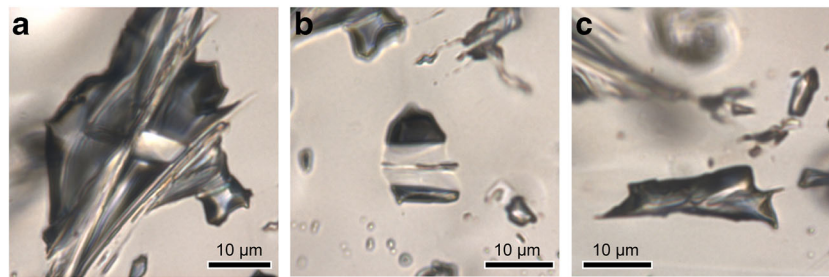


Fig. 1 Photomicrographs of fluid inclusions in andalusite from sample 67E. **a.** large irregular inclusion ($\pm 60 \mu\text{m}$ length) with mica (paragonite-muscovite) and a bright diaspore crystal in the centre. The dark interspace contains a CO_2 -rich gas mixture with minor amounts of CH_4 , N_2 , and H_2 ;

b. equant inclusion ($\pm 15 \mu\text{m}$ length) with about 50 vol.% mica and a CO_2 -rich gas mixture; **c.** elongated dark gas-rich inclusion ($25 \mu\text{m}$ length) without entrapped minerals

Fluid inclusions in leucogranite dyke

Abundant fluid inclusions in various assemblages are observed in andalusite, plagioclase (albite-rich), and quartz from the leucogranite dyke (sample 67E).

Andalusite

Andalusite contains highly irregular-shaped inclusions that have entrapped a gas-mixture and a variety of solid phases (Fig. 1). The size of the inclusions varies between 1 and $50 \mu\text{m}$ in length. The gas phase (Fig. 2, Table 1) is a mixture of CO_2 ($x=0.941$ to 0.983) with minor amounts of CH_4 ($x=0.001$ to 0.026), H_2 ($x=0.000$ to 0.017) and N_2 ($x=0.013$ to 0.034) with a relative high molar volume, which can be deduced from the relative high wavenumbers of individual gases. Microthermometry could not be used for the analyses of these inclusions. Most inclusions contain mica crystals, which are identified as paragonite or muscovite by Raman spectrometry. Diaspore and quartz were detected in some inclusions. The solid phases are not present in all inclusions, and are probably partly accidentally trapped and partly reaction products between originally entrapped aqueous fluid

and andalusite host. At present, none of the inclusions contain H_2O , and it is assumed that part of the mica, diaspore and quartz are most probably reaction products of the reactants H_2O , as subordinate and completely consumed, and andalusite, in excess (e.g., Hemley et al. 1980).

Plagioclase (albite-rich)

Fluid inclusions are highly irregular, either three-dimensional (Fig. 3a) or flat (Fig. 3b). The maximum size of these inclusions is about $20 \mu\text{m}$ in length. Most inclusions reveal a liquid and a vapour phase, whereas in flat inclusions the vapour bubble is usually deformed (i.e., departure from spherical shape) by the limited space, and divided in multiple irregular rounded vapour bubbles. The irregular shape of inclusion walls is often defined by various distinct crystallographical planes (Fig. 3a). The bubbles occupy about 20–25 vol. % of the inclusions. The liquid phase is a nearly pure H_2O solution, and the vapour phase is a gas mixture of CH_4 and H_2 in variable relative amounts. The application of Raman spectroscopy is less useful for these inclusions due to their high fluorescence. Solid phases were not detected in these inclusions.

Fig. 2 The ternary CO_2 - CH_4 - H_2 fluid system with vapour phase compositions in various fluid inclusion assemblages from sample 67E (leucogranite) and 85A (aplite-pegmatite)

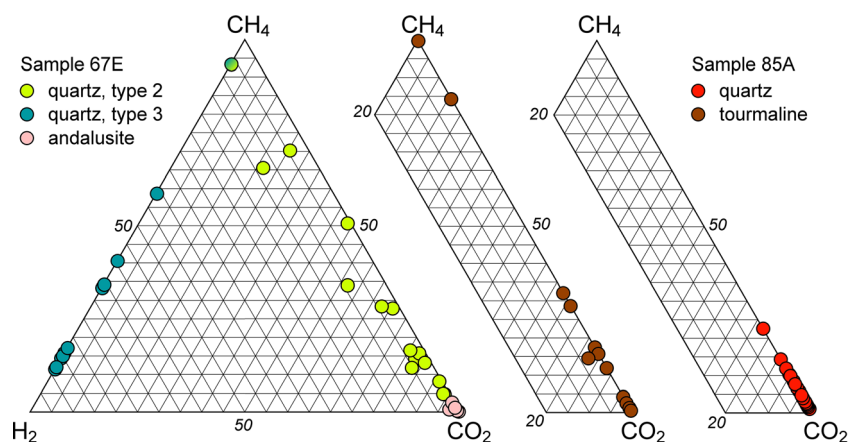


Table 1 Composition of vapour phase of inclusions in andalusite (sample 67E), based on Raman spectroscopy (area Raman peaks)

	Area Raman Peaks					Composition (amount fraction)			
	CO ₂ 1287 cm ⁻¹	CO ₂ 1390 cm ⁻¹	CH ₄ 2918 cm ⁻¹	H ₂ 4156 cm ⁻¹	N ₂ 2330 cm ⁻¹	CO ₂	CH ₄	H ₂	N ₂ *
fi1	24,621	36,415	2952	1868	1644	0.941	0.008	0.017	0.034
fi2	37,085	58,857	2595	990	1198	0.973	0.005	0.006	0.016
fi4	30,446	45,108	5927	366	733	0.971	0.014	0.003	0.013
fi7	36,717	58,711	722	–	1149	0.983	0.001	–	0.016
fi8	23,063	35,254	3485	345	1443	0.955	0.010	0.003	0.032
fi9	29,385	46,492	1197	427	754	0.981	0.003	0.003	0.013
fi10	19,354	29,107	7303	225	785	0.951	0.026	0.003	0.021

* = corrected for atmospheric N₂

Quartz: inclusion type 1

Dens clouds of small sized objects in the centre of quartz crystals were identified as fluid inclusion assemblages. The shape of the outline of these clouds mimics a perfect quartz crystal (Fig. 4a). The individual inclusions are about 1 to 2 μm in diameter, and have a regular equant shape. Most inclusions contain a mica crystal through the centre (Fig. 4b, c). Raman spectroscopy reveals the presence of H₂O and H₂ within the inclusions.

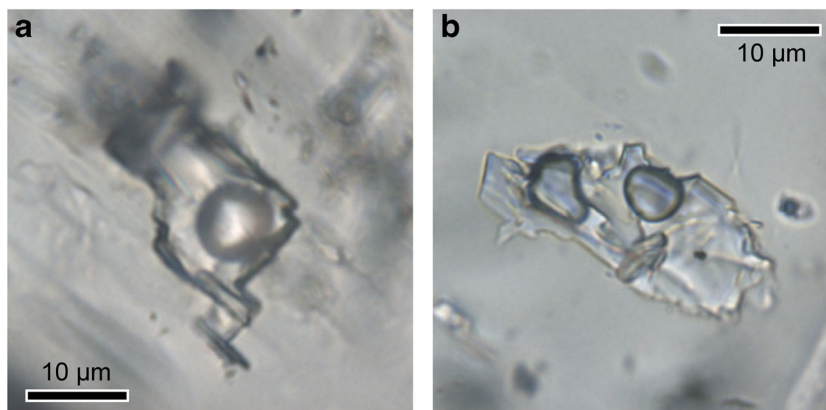
Quartz: inclusion type 2

Inclusions are relative large, 5 to 15 μm in diameter and have a regular and equant shape (Fig. 4d, e). The inclusions are randomly distributed in the quartz crystals. The inclusions contain a liquid and vapour phase, and locally a small solid phase, which is identified as mica by Raman spectroscopy. This phase is interpreted as an accidentally trapped solid due to its limited occurrence. The volume fraction of vapour is about 0.40 ± 0.04 (Electronic Appendix D) and mainly contains CH₄ ($x^{\text{vap}} = 0.081$ to 0.904) and CO₂ ($x^{\text{vap}} = 0.207$ to 0.900) with

minor amounts of H₂ ($x^{\text{vap}} = 0.006$ to 0.125) and N₂ ($x^{\text{vap}} = 0.008$ to 0.035) (Fig. 2). Locally, H₂S and C₂H₆ were detected in only a few inclusions. Raman spectroscopy also illustrates the presence of other C-H vibrations with peaks at 3013 cm⁻¹ and 3065 cm⁻¹ relative wavenumbers. Traces of H₂S (2584 cm⁻¹) were only detected by prolonging the detection time with Raman spectroscopy in only a few inclusions. The liquid phase is a H₂O-rich solution with some minor amounts of dissolved sassolite (H₃BO₃, Raman peak at 875 cm⁻¹) and NaCl. The dissolved NaCl was detected by the formation of hydrohalite at lower temperatures, upon freezing the inclusions according to the method of Bakker (2004) and Baumgartner and Bakker (2010). Raman peaks of hydrohalite were detected at 3405 cm⁻¹, 3422 cm⁻¹, 3437 cm⁻¹ and 3543 cm⁻¹ at -180 °C.

Freezing experiments reveal two nucleation temperatures around -30 °C and -40 °C (Electronic Appendix D) that most probably corresponds to the crystallization of ice and clathrate. During subsequently heating experiments the dissolution of hydrohalite was detected at about -25 °C with Raman spectroscopy. This temperature may correspond to the eutectic temperature of the entrapped fluid

Fig. 3 Photomicrographs of fluid inclusions in plagioclase from sample 67E. **a.** irregular shaped inclusion with a single spherical vapour phase of a CH₄-H₂ mixture. **b.** highly irregular shaped inclusion with multiple vapour phases that are squeezed between irregular inclusion walls



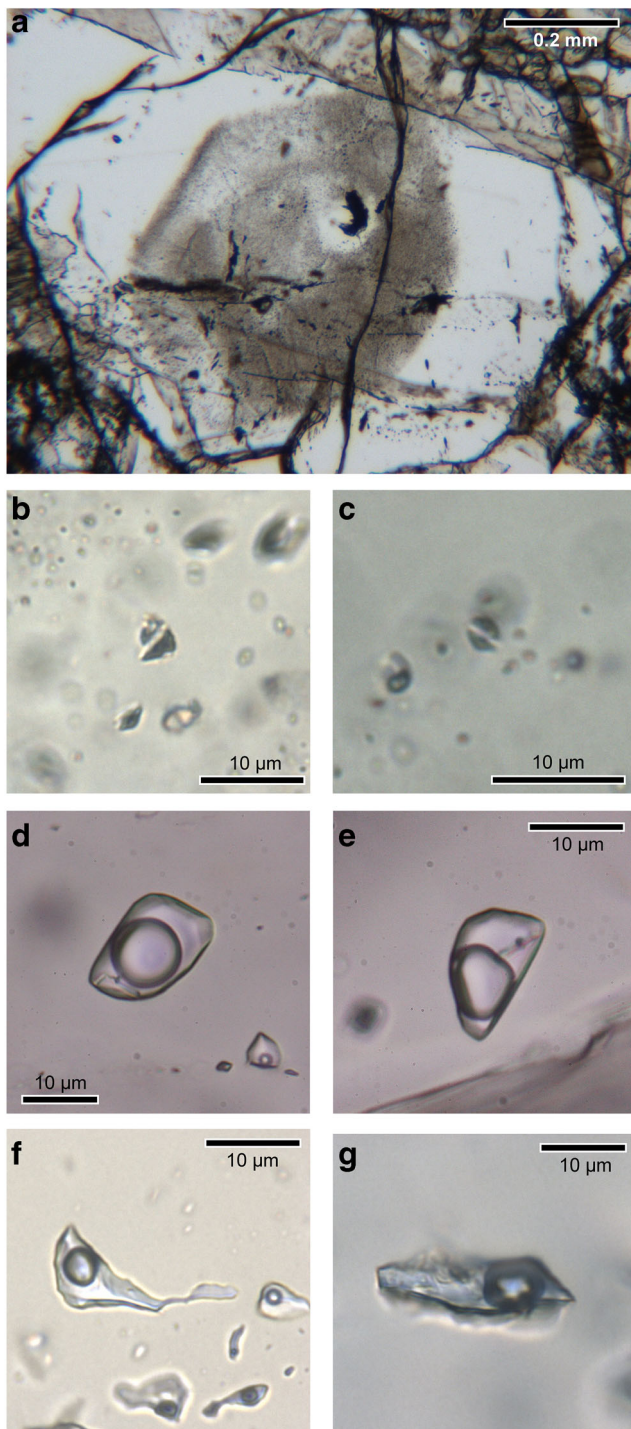


Fig. 4 Photomicrographs of fluid inclusions in quartz from sample 67E. **a.** cloud of an assemblage of *Type 1* fluid inclusions in the centre of a quartz crystal; **b.** and **c.** small regular and equant inclusions of *Type 1* with a mica crystal through the centre, the dark parts of the inclusion contain a mixture of H_2O and H_2 ; **d.** *Type 2* fluid inclusion of about 20 μm diameter with a relative large vapour phase and an accidentally trapped mica, adjacent to a *Type 3* inclusion (lower right corner) which is located in a trail; **e.** *Type 2* fluid inclusion; **f.** irregular shaped *Type 3* fluid inclusions with traces of necking processes; **g.** elongated irregular shaped *Type 3* fluid inclusion

system. The final dissolution of ice occurs at variable temperatures between -7.6 and -2.2 $^{\circ}C$ (Fig. 5a, b), and clathrate (gas hydrate) completely dissolves at higher temperatures between $+6$ and $+12$ $^{\circ}C$. Homogenization of liquid and vapour phase occurs in a narrow temperature range at 370 – 380 $^{\circ}C$ (mode in Fig. 5a, c) in the liquid phase, illustrating homogenous trapping conditions for *Type 2* fluid inclusion assemblages.

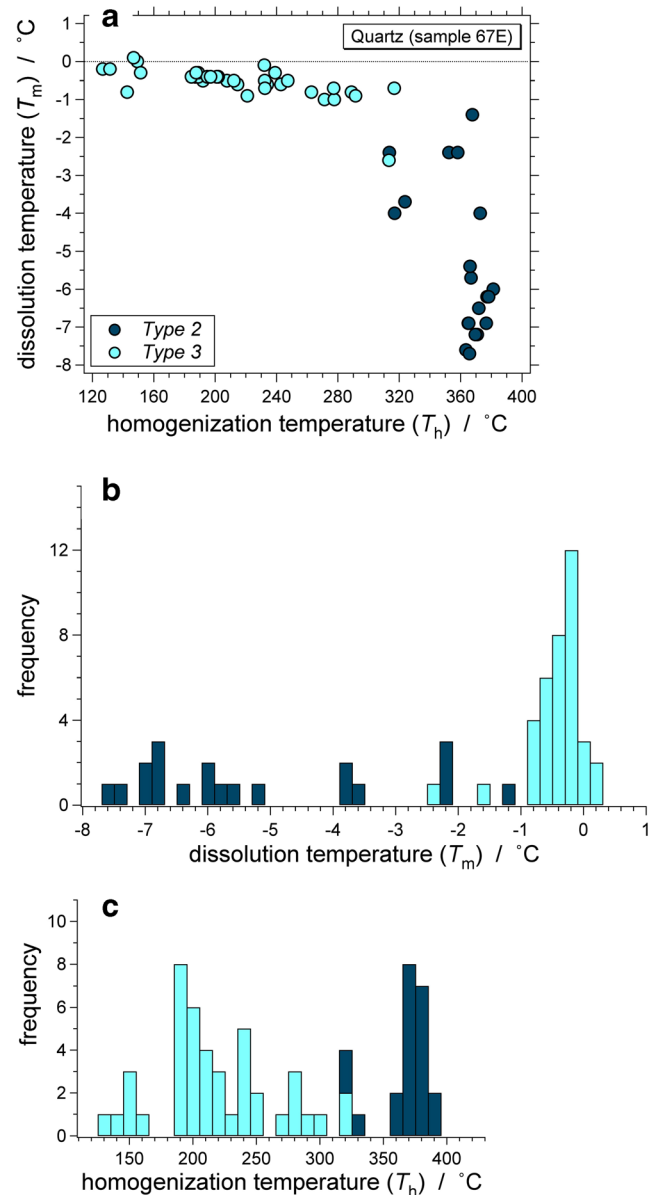


Fig. 5 Homogenization temperatures (LV \rightarrow L) and ice dissolution temperatures of *Type 2* ($LS_{ice}S_{cla}V \rightarrow LS_{cla}V$) and *Type 3* ($LS_{ice}S_{cla}V \rightarrow LV$) fluid inclusion assemblages in quartz from sample 67E. **a.** correlation between homogenization and dissolution temperatures; **b.** histogram ice dissolution temperatures; **c.** histogram homogenization temperatures

Quartz: inclusion type 3

The inclusions occur in trails and have irregular elongated shapes (Fig. 4f, g). The inclusions contain a liquid and vapour phase with a highly variable volume fraction between 0.05 and 0.31, with a mean value of 0.16 (Electronic Appendix E). Locally an opaque mineral was identified as anatase with Raman spectroscopy. The result of necking processes after nucleation of the vapour phase within individual inclusions during geological cooling processes is illustrated by inclusions with a large vapour volume fraction adjacent to inclusions with small volume fractions or all-liquid inclusions (Fig. 6). Also narrow channels between irregular shaped inclusions that separate a vapour-rich part from a part with only a liquid phase may illustrate an incomplete necking process (Fig. 4f).

The vapour phase consists of a gas mixture of CH₄ and H₂ (Electronic Appendix E, Fig. 2), and the liquid phase is nearly pure H₂O with minor amounts of NaCl, which cannot be detected by cryo-Raman spectroscopy, but can be inferred from melting-point depression of ice. These fluid properties are similar to the above mentioned fluids in plagioclase. Freezing the inclusions result in ice nucleation between -40 to -28 °C. The final dissolution of ice occurs at an average value of -0.6 °C (sd. ±0.5, mode at -0.2 °C, see Fig. 5a, b), which illustrates a homogeneous and low salinity. Clathrate dissolution temperatures are difficult to detect optically and appear to nearly coincide with ice dissolution temperatures, according to cryo-Raman spectroscopic monitoring. The total homogenization temperature is highly variable, between 130 and 320 °C, with a mode at 180 °C (Fig. 5a, c). This variability may reflect a gradual evolution of trapping conditions of a specific fluid system, in addition to necking processes.

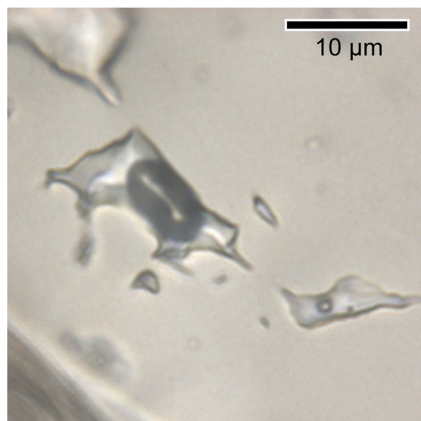


Fig. 6 Photomicrographs of *Type 3* fluid inclusions in quartz from sample 67E, with variable volume fractions of the vapour phase as a result of necking processes after phase separation

Fluid inclusions in aplite-pegmatite dyke

Abundant fluid inclusions in various assemblages are observed in tourmaline and quartz from the aplite-pegmatite dyke (sample 85A).

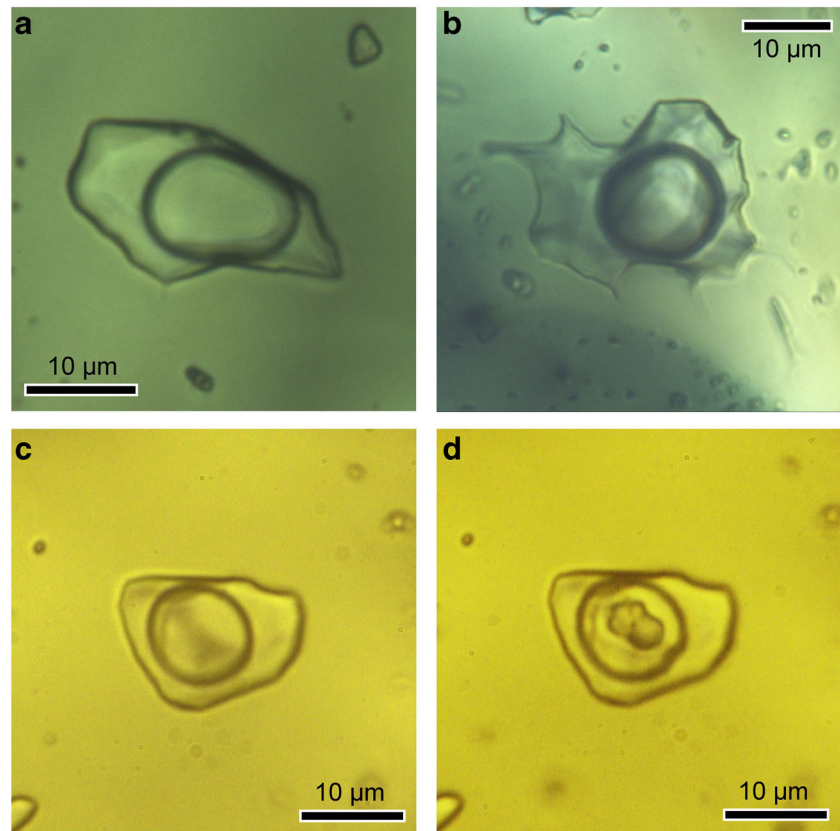
Tourmaline

The tourmaline contains exceptional large fluid inclusions (up to 40 μm in length), which have equant shapes, either regular or irregular (Fig. 7a, b), in great contrast to the narrow and extremely elongated tube-like inclusions described in miarolitic cavities by Ruggieri and Lattanzi (1992, c.f. Fig. 5f therein). Flat inclusions have a regular shape, whereas three-dimensional equant inclusions are irregular. Both types contain similar fluids. The inclusions occur mainly in the core of tourmaline crystals with a foitic composition. The inclusions contain a liquid and vapour phase of about 41 vol. % (average value Electronic Appendix F), and locally a sassolite crystal (H₃BO₃, Raman peaks at 880 and 500 cm⁻¹, see Janda and Heller 1979) at room temperature. Sassolite is metastable absent in numerous fluid inclusions at room temperature, and can be nucleated with laser irradiation (532.068 nm, 1–2 mW) from the Raman spectrometer (Fig. 7c, d). Some inclusions contain a small arsenolite crystal (As₄O₆, Raman peaks at 268, 369 and 559 cm⁻¹) or arsenic crystal (Raman peak at 253 cm⁻¹). The vapour phase consist of a low-density gas mixture of mainly CO₂ and CH₄ and locally traces of H₂S, N₂ and H₂ (Fig. 2, Table 2), which can only be detected by Raman spectroscopy in inclusions that are located close to the surface of the sample. The properties of individual fluid inclusions are given in the Electronic Appendix F.

Freezing experiments results in the nucleation of ice and clathrate in fluid inclusions. Final ice dissolution temperatures are at a mode of -7.0 °C and may reach temperatures as high as 0.0 °C in some inclusions (Fig. 8a, b). Clathrate dissolution can only be detected by cryo-Raman spectroscopy, and occurs at similar temperatures, which correspond to approximately Q_1 conditions (Bakker et al. 1996). Sassolite dissolution occurs in the range of +8.6 to +25.7 °C. Total homogenization of liquid and vapour phases occurs at a mode of 380 °C in the liquid phase (Fig. 8a, c) in a relative narrow temperature range.

Close examination of these results reveals the possibility to subdivide these fluid inclusions into two groups (Fig. 8, Table 2): 1. inclusions that contain a sassolite crystal, or inclusions that nucleate a sassolite crystal upon laser irradiation (*Group D* in Table 2); 2. inclusions that do not contain sassolite (*Group A* in Table 2). The Raman signal of the vapour phase in the first group (*D*) is extremely weak, and reveals a variable CO₂ amount fraction between 0.78 and 0.98. In some

Fig. 7 Photomicrographs of fluid inclusions in tourmaline from sample 85A. **a.** relative flat regular shaped inclusion; **b.** irregular fluid inclusion with a spherical vapour phase illustrating its equant shape; **c.** and **d.** regular shaped inclusion before and after laser irradiation, respectively, that causes the nucleation of a sassolite crystal at the liquid-vapour boundary



inclusions traces of N_2 were detected. The low intensity of the Raman signal results in significant uncertainties in composition calculations. The homogenization temperatures are slightly higher than the other group, whereas the dissolution temperatures of ice are slightly lower (Fig. 8a, b). Inclusions from the other group (*A*) have a much stronger Raman signal of the vapour phase, which is highly enriched in CO_2 , and contain locally H_2S up to $x^{vap}=0.02$. In addition to these groups, some inclusions reveal higher fractions of CH_4 (up to $x^{vap}=0.67$) and N_2 (up to $x^{vap}=0.15$), *Group B* and *Group C* in Table 2. *Group C* is related to *Group D* because the aqueous liquid solution contains minor amounts of dissolved sassolite, and the vapour phase has a relative strong Raman signal. *Group B* is related to *Group A* because sassolite is absent, and some inclusions contain H_2 up to $x^{vap}=0.03$.

Quartz

The quartz contains abundant fluid inclusions, which are homogeneously distributed within single grains (Fig. 9a). The inclusion shape is highly variable, from regular and equant (Fig. 9b, c) to irregular and elongated (Fig. 9d). The inclusion size may vary from 1 μm up to 40 μm in length. The inclusions contain a liquid phase and a vapour phase of 0.183 volume fraction (s.d. 0.014, Electronic Appendix G), with

locally accidentally trapped mica. The liquid phase is a H_2O -rich solution with traces of dissolved sassolite, mainly detectable as a weak Raman peak at about 880 cm^{-1} . The vapour phase is a low-density gas mixture of CO_2 (Fig. 2) and minor amounts of CH_4 (up to $x^{vap}=0.22$). The low intensity of the Raman signal results in significant uncertainties in these composition calculations. Microthermometry illustrates a homogeneous fluid inclusion assemblage (Fig. 10). Upon freezing of the inclusions, only ice can be nucleated, which completely dissolves at about $-2.8\text{ }^\circ C$ (mode value in Fig. 10a, b). Clathrates and salt-hydrates were not observed at low temperatures. Total homogenization occurs in to the liquid phase at a mode of $240\text{ }^\circ C$, within a range of 200 to $290\text{ }^\circ C$ (Fig. 10a, c). A complete list with the measured properties of individual fluid inclusions in quartz is given in the Electronic Appendix G.

Discussion

Calculation of fluid properties leucogranite dyke

The bulk fluid properties of *Type 2* fluid inclusions in quartz from sample 67E can be calculated with the program *ICE* (Table 3). These calculations are based on knowledge of ice

Table 2 Calculated composition of vapour phase from Raman peak analyses of fluid inclusions in tourmaline (Sample 85A). *solid* illustrates Raman-detected solid phases within individual inclusions (*sas* = sassolite). *aq.* is dissolved in H₂O. *int.* is the relative intensity of the Raman spectra of gas mixtures: s = strong; w = weak

Sample 85A tourmaline		Composition vapour phase					Solid	Int.
		x(CO ₂)	x(CH ₄)	x(H ₂ S)	x(N ₂)	x(H ₂)		
Group A	fi40	0.997	0.003	–	–	–	–	s
	fi41	0.996	0.004	–	–	–	–	s
	fiu	0.996	0.004	–	–	–	–	s
	fis	0.995	0.005	–	–	–	–	s
	fit	0.992	0.008	trace	–	–	–	s
	fiq	0.970	0.008	0.022	–	–	–	
	fir	0.954	0.025	0.021	–	–	–	s
	fiw	0.944	0.056	–	–	–	–	s
	fim	0.867	0.133	trace	trace	–	–	
Group B	fie	0.956	0.044	–	trace	–	arsenic	w
	fiF	0.826	0.145	–	–	0.029	–	s
	fiy	0.816	0.109	–	0.075	–	–	
	fi0	0.714	0.286	–	–	–	–	s
Group C	fik	0.125	0.672	–	0.203	–	–	s
	fil	0.989	0.011	–	–	–	sas(aq)	s
	fii	0.944	0.022	–	0.035	–	sas(aq)	s
Group D	fin	0.561	0.265	0.021	0.153	–	sas(aq)	s
	fic	0.985	0.015	–	trace	–	sas	w
	fid	0.981	0.019	–	trace	–	sas	w
	fi30	0.980	0.020	–	–	–	sas	w
	fib	0.959	0.041	–	–	–	sas	w
	fi27	0.927	0.073	–	–	–	sas	w
	fi4	0.893	0.107	–	–	–	sas	w
	fiV	0.843	0.157	–	–	–	sas	w
	fia	0.826	0.174	–	–	–	sas	w
fi2	0.777	0.223	–	–	–	sas	w	

and clathrate dissolution temperatures and volume fractions of the vapour phase. Furthermore, the minor amounts of N₂ and H₂ are combined due to similarities in gas properties, and the minor amount of dissolved sassolite is neglected. The inclusions are highly enriched in H₂O ($x=0.911$ to 0.958). Sassolite can only account for -0.7° of dissolution point depression of ice (e.g., Peretyazhko et al. 2000). Therefore, dissolution point depression is assumed to result mainly from the presence of dissolved NaCl. The CO₂ amount fraction varies between 0.029 and 0.068. The inclusions that are relatively enriched in CH₄ ($x=0.015$ to 0.033) reveal the highest H₂O content. N₂ and H₂ only occur in very low concentrations ($x=0.001$ to 0.003). The salinity is relatively low, varying between 2.83 and 7.02 eq. mass% NaCl. The molar volume of the vapour phase is precisely defined at the clathrate dissolution temperature whereas the bulk molar volume is highly dependent on the estimation of volume fraction of the vapour phase at room temperatures. The small spread in homogenization temperature of *Type 2* fluid inclusions in sample 67E suggests only minor difference in bulk densities and, therefore, similar volume fractions. Fluid inclusions with a vapour

area fraction of 0.43 to 0.44 are assumed to represent accurate estimates of true volume fractions (c.f. average value 0.40, see Electronic Appendix D), therefore, the bulk molar volume of these inclusions may only vary between 30.43 and 31.70 cm³ · mol⁻¹, i.e., 0.619 to 0.649 g · cm⁻³.

The *Type 3* fluid inclusions in quartz from sample 67E contain a low density CH₄-H₂-rich gas mixture in the vapour phase. The existence of H₂ in clathrates has only been recently discovered (e.g., Struzhkin et al. 2007), and is not yet included in mixed-gas clathrate stability models. H₂ clathrate is stable at pressures exceeding 100 MPa, therefore, only CH₄ is taken into account in the present study to calculate Q_1 dissolution conditions (program ICE) of fluid inclusions (Table 4). The fluid inclusions are extremely enriched in H₂O ($x=0.990$ to 0.996), with only minor amounts of gas components CH₄ and H₂ ($x=0.004$ to 0.009), whereas the salinity can be neglected (Table 4). The molar volume of the gas mixture in the vapour phase is 805 ± 5 cm³ · mol⁻¹. The variability in homogenization temperatures illustrates a highly variable bulk density. Approximate bulk densities (or bulk molar volumes) can also be calculated from homogenization temperatures assuming a

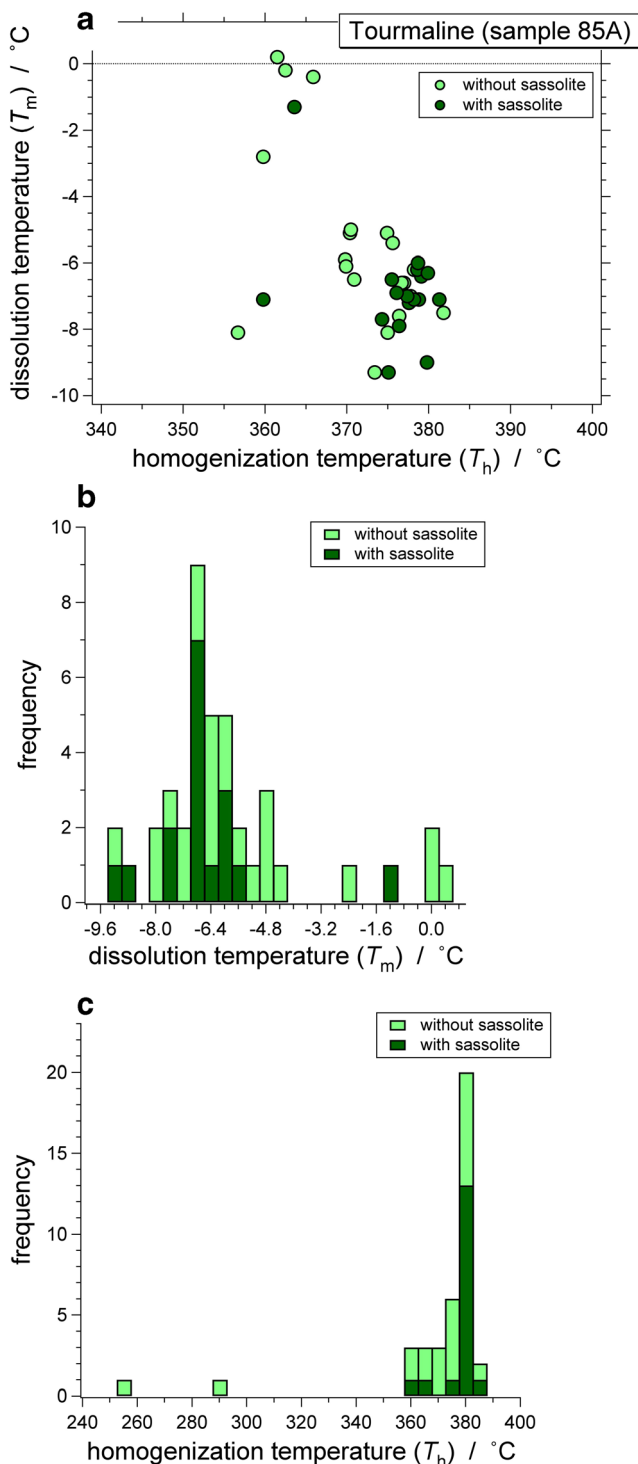


Fig. 8 Homogenization temperatures (LV → L) and ice dissolution temperatures (LS_{ice}S_{cla}S_{sas}V → LS_{sas}V or LS_{ice}S_{cla}V → LV) of fluid inclusion assemblages in tourmaline from sample 85A. **a.** correlation between homogenization and dissolution temperatures; **b.** histogram ice dissolution temperatures; **c.** histogram homogenization temperatures

pure H₂O fluid (with *Loner HGK*), neglecting the small amounts of gas and salt in the system. These numbers are per definition slightly higher than values calculated with the

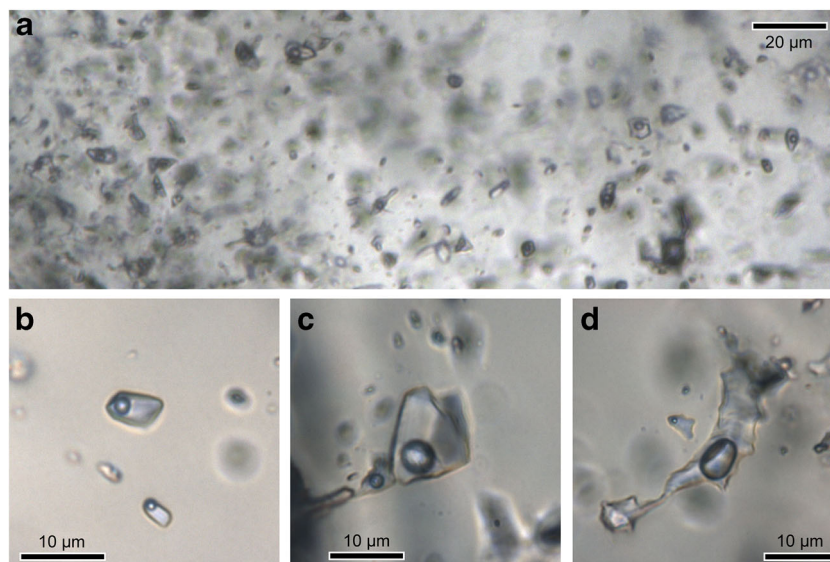
program *ICE* due to the effect of adding small amounts of gas and salt to H₂O-rich solutions. Adding 1 amount % of CH₄ to a hypothetical pure H₂O system results in a molar volume decrease of 2 % at a specific constant T_h value (modelled with program *Loner 9*, Bakker 2003). Adding 1 amount % of NaCl results in a molar volume decrease of 1 % (modelled with program *AqSo DH*). Furthermore, the uncertainty in vapour volume fraction estimations as describe in the previous paragraph must be taken into account, but is supposed to be much smaller due to the relative small fraction of the vapour phase. The fluid inclusions *fi14*, *fi15*, *fi16*, *fi58* and *fi62* (Table 4) may reflect the majority of *Type 3* inclusions (c.f. mode value and spread in Fig. 5c), corresponding to a molar volume variation between 20.01 and 22.75 cm³ · mol⁻¹ (0.793 to 0.901 g · cm⁻³).

Calculation of fluid properties aplite-pegmatite dyke

Concentrations of H₃BO₃ in natural and synthetic inclusions can be estimated with Raman spectroscopy (e.g., Thomas 2002; Sirbescu et al. 2013), and microthermometry (e.g., Peretyazhko et al. 2000) using purely empirical models. Data obtained by microthermometry can also be thermodynamically analysed with a mixed-solvent electrolyte model that is combining the Pitzer-Debye-Hückel model of osmotic coefficients, UNIQUAC equations and the Helgeson-Kirkham-Flowers equation of state (see details in Wang et al. 2013). Analytical limitations and uncertainties of both Raman spectra analyses and microthermometry cannot be specified due to multiple types of dissolved ions in H₂O that result in the same variability of measured parameters (i.e., wavenumber intensity and temperatures). For example, the dissolution temperature of ice lower than 0 °C can be caused by a large variety of ions, therefore, T_m (ice) cannot be used directly to identify the type of dissolved ions. However, the nucleation of salt-hydrates at low temperatures that are detected by Raman spectroscopy can be used to identify the major dissolved components (e.g., Bakker 2004; Baumgartner and Bakker 2010). Therefore, the use of equivalent concentrations (usually of NaCl) is a well-accepted limitation in fluid inclusion research.

Ice and sassolite dissolution temperatures have been measured in single inclusions in the present study in tourmaline (Electronic Appendix F), and can be directly used to calculate H₃BO₃ concentration and equivalent NaCl concentrations in the ternary H₂O-NaCl-H₃BO₃ system. The presence of boric acids (sassolite) in fluid and melt inclusions has been reviewed by Peretyazhko et al. (2000, and reference therein). They collected data of the ternary H₂O-NaCl-H₃BO₃ system and presented a solubility diagram (i.e., liquidus) that can be used to determine the composition from dissolution temperatures at cotectic conditions and final dissolution in the ice-field, hydrohalite-field and partly in the sassolite-field and halite-

Fig. 9 Photomicrographs of fluid inclusions in quartz from sample 85A. **a.** overview of the distribution of abundant fluid inclusions in quartz; **b.** regular and slightly elongated fluid inclusions ($\pm 7 \mu\text{m}$ length) with a vapour and liquid phase. **c.** regular equant fluid inclusions ($\pm 10 \mu\text{m}$ diameter). **d.** irregular elongated inclusion ($\pm 30 \mu\text{m}$ length)



field (Fig. 11). We have used these data to construct a new ternary diagram (in mass%) to estimate graphically the composition of the aqueous liquid solution of fluid inclusions in tourmaline (Table 5). Isotherms and cotectic lines within these fields are newly defined by purely empirical equations to be able to interpolate the microthermometrical results (Electronic Appendix H). The average composition and standard deviation in mass fractions illustrated in Table 5 is 0.859 ± 0.011 for H_2O , 0.099 ± 0.011 for NaCl , and 0.042 ± 0.007 for H_3BO_3 .

The bulk composition and molar volume of fluid inclusions in tourmaline are obtained by adding the properties of vapour and liquid phase, using their volume fraction estimations. The composition of the vapour phase is estimated by analyses of Raman spectra, and the density is obtained by knowledge about clathrate dissolution temperatures, which was only seldomly observed but similar to $T_{\text{m}}(\text{ice})$. The program *ICE* can only be used to calculate bulk fluid properties at Q_1 conditions with specific simplifications of the chemical system in these inclusions: 1. the gas-mixture contains only CO_2 and CH_4 ; 2. the $T_{\text{m}}(\text{ice})$ depression is only caused by the presence of gases and NaCl (equivalent salinity); and 3. the volume fraction of the vapour phase is equal to the area fraction in projected images. The inclusions *fi27* and *fi30* (Table 2, Electronic Appendix F) have been selected to illustrate calculated bulk fluid properties. At Q_1 clathrate dissolution conditions, the vapour phase has a molar volume of 2280 to $2325 \text{ cm}^3 \cdot \text{mol}^{-1}$ (0.0184 to $0.0187 \text{ g} \cdot \text{cm}^{-3}$). The bulk amount fractions of H_2O , CO_2 , CH_4 and NaCl are 0.9582, 0.0159–0.0174, 0.0001–0.0004, and 0.0243–0.0255, respectively. The bulk molar volume varies between 29.06 and $31.03 \text{ cm}^3 \cdot \text{mol}^{-1}$ (0.612 to $0.653 \text{ g} \cdot \text{cm}^{-3}$). This calculation procedure can be used for inclusions with and without sassolite daughter crystals. The bulk composition with equivalent amounts of NaCl can be modified according to the

presence of sassolite. Comparison of Table 5 with values calculated in the binary H_2O - NaCl equivalent system using only $T_{\text{m}}(\text{ice})$, illustrates that the amount of H_2O and NaCl are a factor 0.9876 and 0.9550 smaller, respectively, whereas H_3BO_3 is about 29 % of the total amount of dissolved ions in H_2O . The final bulk composition is, therefore, $x(\text{H}_2\text{O}) = 0.9463$; $x(\text{CO}_2) = 0.0159$ to 0.0174 ; $x(\text{CH}_4) = 0.0001$ to 0.0004 ; $x(\text{NaCl}) = 0.0232$ to 0.0244 ; $x(\text{H}_3\text{BO}_3) = 0.0095$ to 0.0099 .

Raman spectroscopy has been proposed to be the best method to estimate H_3BO_3 concentrations in aqueous liquid solution in fluid and melt inclusions (e.g., Thomas 2002; Sirbescu et al. 2013). In principle, Raman spectroscopy is not designed to detect amount fractions, but trends in the shift and shape of specific vibrational bands can be used for purely empirical modelling of concentrations (e.g., Burke 2001). However, quantification of concentrations in fluid phases with Raman spectroscopy always results in poorly defined uncertainties because spectra have to be compared to standard spectra, which are highly variable for fluid inclusions due to host mineral properties, size-shape-depth properties of inclusions, and specific instrument factors (e.g., Baumgartner and Bakker 2009; Sirbescu et al. 2013). The use of intensity of specific wavenumbers of individual fluid components (e.g., H_2O) has been a popular method to estimate concentration (e.g., Mernagh and Wilde 1989; Thomas 2002), however the spectrum of H_2O is a broad band between 2900 and 3800 cm^{-1} relative wavenumbers, and the selected wavenumber is completely arbitrarily and does not represent or coincide with fundamental parameters that define the shape of a H_2O -spectrum. Moreover, the H_2O spectrum is influenced by all dissolved species, and the effect of individual ions cannot be deduced from one spectrum. Similar arguments were originally used against the method of microthermometry, and were the

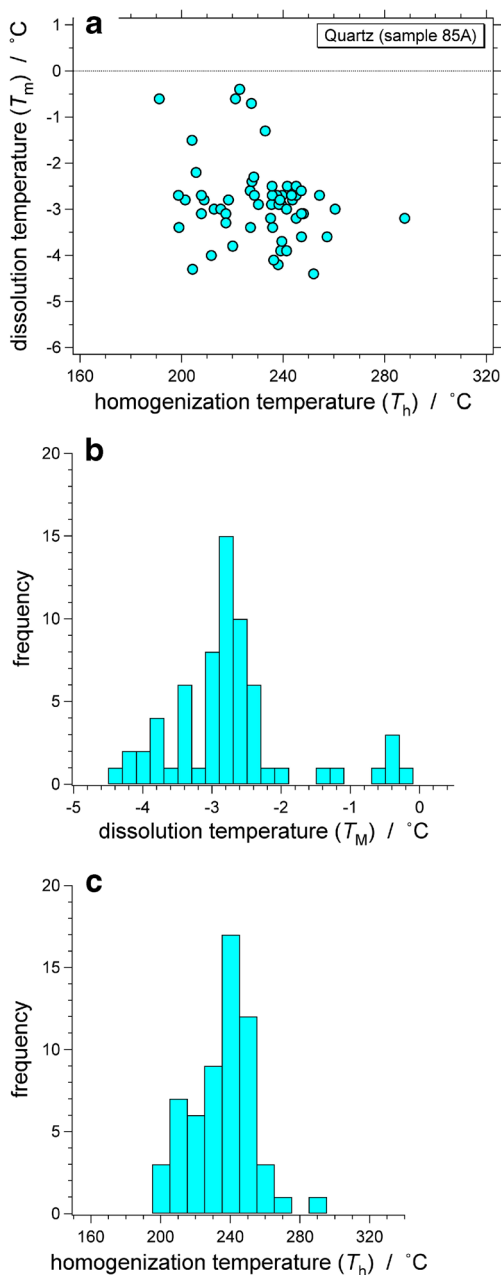


Fig. 10 Homogenization temperatures (LV → L) and ice dissolution temperatures ($LS_{ice}V \rightarrow LV$) of fluid inclusion assemblages in quartz from sample 85A. **a.** correlation between homogenization and dissolution temperatures; **b.** histogram ice dissolution temperatures; **c.** histogram homogenization temperatures

justification for the new approach using Raman spectroscopy. However, the uncertainties of temperature measurements are much better defined than the above-mentioned Raman analyses, and the properties of fluid phase diagrams of multi-component systems can be modelled according to fundamental thermodynamic principles (Wang et al. 2013).

Properties of fluid inclusions in quartz from sample 85A can be modelled according to the same method as described for inclusions in tourmaline. However, the absence of

clathrates and salt hydrates due to low concentrations of gases and salts reduces calculation procedures with the program *ICE* to limiting conditions. Calculations can only be performed by assuming Q_1 dissolution conditions where both ice and clathrate dissolve at the same temperature. These conditions define minimum molar volumes of the gas-mixture in the vapour phase and maximum concentrations of gases and salts in the bulk fluid inclusion. The results of selected fluid inclusions from Electronic Appendix G are illustrated in Table 6. The average composition in amount fractions is 0.9773 ± 0.0026 for H_2O , 0.0145 ± 0.0006 for CO_2 , 0.0002 ± 0.0001 for CH_4 , and 0.0080 ± 0.0026 for $NaCl$, with a molar volume of $22.55 \pm 0.63 \text{ cm}^3 \cdot \text{mol}^{-1}$. Furthermore, the inclusions contain minor amounts of H_3BO_3 , which are extremely low and cannot be specified with microthermometry or Raman spectroscopy.

The total homogenization temperatures have not been used in the above mentioned calculation procedures with the program *ICE*. This temperature is mainly defining the bulk molar volume of each fluid inclusion. *fi21* from *Qtz1* (Table 6) is used to illustrate that a pure H_2O fluid systems is a good approximation of the bulk fluid properties. The T_h of 245.1 °C in the liquid phase (see data in Electronic Appendix G) corresponds to $22.34 \text{ cm}^3 \cdot \text{mol}^{-1}$ for a pure H_2O fluid (program *Loner HGK*). This temperature corresponds to slightly lower V_m ($21.90 \text{ cm}^3 \cdot \text{mol}^{-1}$) if small amounts of $NaCl$ are taken into account (program *AqSo DH*). In contrast, slightly higher V_m values are obtained if small amounts of gases are taken into account. This relative change in T_h - V_m paired values can be modelled with the program *Loner B*. Therefore, the presence of minor amounts of both CO_2 and $NaCl$ does not effect molar volume calculations from T_h according to a pure H_2O fluid system, which greatly simplifies isochore calculations.

The effect of B, Li, and F on microthermometrical properties and isochore calculations

The effect of adding small amounts of $NaCl$ to pure water solutions has been well documented (e.g., Driesner 2007; Driesner and Heinrich 2007, and reference therein) and include, for example, freezing point depression of water, adjustment of isochores, and the development of a large liquid-vapour immiscibility field at higher temperatures and pressures. B, Li, and F may also affect these properties of water-rich solutions in a similar way.

The modification of dissolution temperatures of ice in ternary H_2O - $NaCl$ - H_3BO_3 solution is modelled in the preceding paragraph, according the data presented by Peretyazhko et al. (2000). The modification of the slope of pure H_2O isochores by adding H_3BO_3 and NaF was illustrated by Peretyazhko and Zagorsky (2002) and Peretyazhko (2009), respectively. The presence of H_3BO_3 in solution raises the critical point of the H_2O -rich solution, but also changes the slope of isochores, a

Table 3 Calculated properties of vapour phase (composition and molar volume) and bulk fluid properties of *Type 2* inclusions in quartz from sample 67E. *gas** is the sum of the amount of H₂ and N₂

	composition vapour (Raman)				V _m (vap) cm ³ /mol	Bulk properties (program ICE)						
	x(CO ₂)	x(CH ₄)	x(H ₂)	x(N ₂)		x(H ₂ O)	x(CO ₂)	x(CH ₄)	x(gas*)	x(NaCl)	V _m cm ³ /mol	mass% NaCl
fi1	0.900	0.081	0.006	0.013	456.8	0.927	0.051	0.003	0.001	0.019	31.15	6.12
fi3	0.806	0.144	0.028	0.021	–	–	–	–	–	–	–	–
fi4	0.815	0.117	0.050	0.018	370.8	0.924	0.053	0.004	0.002	0.016	30.43	5.40
fi5	0.474	0.495	0.006	0.025	316.6	0.934	0.029	0.015	0.001	0.022	26.60	7.02
fi6	0.670	0.280	0.038	0.012	–	–	–	–	–	–	–	–
fi7	0.694	0.276	0.015	0.016	338.7	0.922	0.050	0.012	0.001	0.015	31.70	4.87
fi8	0.817	0.156	0.015	0.012	427.5	0.929	0.048	0.005	0.001	0.017	30.58	5.47
fi9	0.846	0.132	0.014	0.008	334.3	0.925	0.051	0.004	0.001	0.019	27.66	6.25
fi19	0.249	0.693	0.043	0.015	170.6	0.933	0.021	0.033	0.003	0.009	25.05	3.13
fi21	0.207	0.638	0.125	0.029	–	–	–	–	–	–	–	–
fi34	0.921	0.047	0.010	0.022	391.4	0.927	0.049	0.001	0.001	0.021	28.04	6.97
fi37	0.910	0.048	0.012	0.030	299.3	0.911	0.068	0.002	0.002	0.016	31.35	5.48
fi39	0.555	0.332	0.086	0.027	–	–	–	–	–	–	–	–
fi64	0.781	0.163	0.030	0.027	–	–	–	–	–	–	–	–
fi23	–	0.904	0.062	0.035	276.13	0.958	–	0.030	0.003	0.009	25.97	2.83

similar effect as known for NaCl. The isochore slope of H₃BO₃ bearing solutions is less steep for relative high-density fluids with homogenization temperatures below approximately 300 °C, and is steeper for less dense fluids (c.f. Fig. 1. in Peretyazhko and Zagorsky 2002; and Fig. 4.4 in Shepherd et al. 1985) than the isochores of pure water at the same homogenization conditions. The slope of relative low density NaF bearing solutions (vapour-like) increase with higher concentrations of NaF, which is, again, similar to modifications obtained in low density fluids by H₃BO₃ and NaCl.

The calculated amount fraction of H₃BO₃ in fluid inclusions in the leucogranite dyke and aplite-pegmatite dyke is lower than 4.2 %. Peretyazhko and Zagorsky (2002) illustrated that boric acid solution with less than 13 mass% H₃BO₃ (=4.2 amount%) do not significantly affect the slope of isochores. Lithium and fluorine were not identified in any of the fluid inclusion assemblages, but they may be dissolved in minor amounts in the aqueous solutions of the Mt. Capanne plutonic complex. Lithium was not identified in tourmaline from the analyzed samples, which have a foitic to schorlitic composition (Electronic Appendix C). Low concentrations of

Table 4 Calculated properties of vapour phase (composition and molar volume) and bulk fluid properties of *Type 3* inclusions in quartz from sample 67E. *gas** is the sum of the amounts of CH₄ and H₂. V_m (HGK) is the calculated molar volume of pure H₂O fluids based on homogenization temperatures using program *Loner HGK*

	composition vapour (Raman)		V _m (vap) cm ³ /mol	Bulk properties (program ICE)					V _m (HGK) cm ³ /mol
	x(CH ₄)	x(H ₂)		x(H ₂ O)	x(gas*)	x(NaCl)	V _m cm ³ /mol	mass% NaCl	
fi2	0.588	0.412	801.5	0.994	0.005	0.001	20.69	0.37	21.06
fi10	0.406	0.594	812.7	0.990	0.006	0.004	21.93	1.16	23.53
fi12	0.115	0.885	805.9	0.989	0.009	0.002	24.26	0.69	26.67
fi14	0.144	0.856	801.5	0.995	0.004	0.001	20.01	0.37	20.61
fi15	0.154	0.846	803.7	0.992	0.007	0.002	22.20	0.53	22.26
fi16	0.157	0.843	–	–	–	–	–	–	–
fi27	0.118	0.882	797.1	0.994	0.005	0.000	21.16	0.05	–
fi42	0.333	0.667	808.2	0.992	0.005	0.003	20.93	0.84	23.11
fi57	0.172	0.828	797.1	0.996	0.004	0.000	20.00	0.05	19.67
fi58	0.152	0.848	803.7	0.994	0.004	0.002	20.45	0.53	21.27
fi62	0.343	0.657	805.9	0.991	0.007	0.002	22.75	0.69	21.87

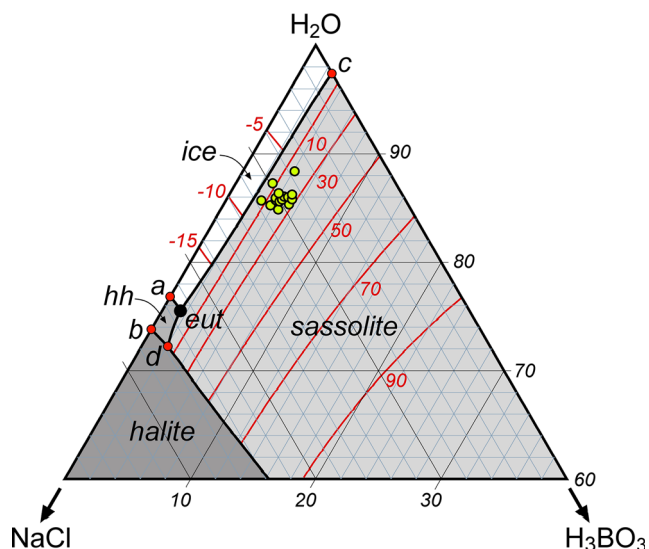


Fig. 11 Vapour saturated liquidus surface in the ternary H_2O - NaCl - H_3BO_3 system in mass fractions (numbers along axes in mass %). The four fields *ice*, *sassolite*, *hydrohalite* (*hh*), and *halite* represent the stability of these solids with an aqueous liquid solution and a vapour. The fields are separated by cotectic curves (*black solid curves*) that are mathematically defined in Appendix H. The *red solid curves* are isotherms (in $^\circ\text{C}$) of final dissolution temperatures of the solid phases in the aqueous liquid solution. *eut* is the eutectic point of the ternary system at -21.4°C , 23.02 mass% NaCl and 1.46 mass% H_3BO_3 . The points *a* and *b* are the eutectic and peritectic point, respectively, of the binary H_2O - NaCl system. Point *c* is the eutectic point of the binary H_2O - H_3BO_3 system, and *d* is the shifted peritectic in H_3BO_3 -bearing systems. *Green circles* are the experimental data obtained from fluid inclusions in tourmaline from sample 85A (Appendix F)

lithium and fluorine do not have a measurable effect on the microthermometric properties of water-rich fluids, and do not change significantly the slope of isochores.

Arsenic in fluid inclusions in tourmaline, aplite-pegmatite dyke

Arsenolite and native arsenic have only been detected in some inclusions in tourmaline (Electronic Appendix F) and may, therefore, be regarded as accidentally trapped crystals during the formation of homogeneous fluid inclusion assemblages. The presence of arsenic was described for rhyolitic peraluminous glass and melt inclusions in granite-pegmatite hydrothermal systems (e.g., Borisova et al. 2010; Rickers et al. 2006) and only few studies report the presence of arsenic in hyper-saline fluid inclusions and polyphase fluid inclusions (e.g., Rickers et al. 2006; James-Smith et al. 2010; Anderson and McCarron 2011).

Arsenolite is highly soluble in hydrothermal fluids at high temperatures and pressures (Pokrovski et al. 1996), and may develop daughter crystals in numerous fluid inclusion assemblages. The absence of sulphur in these pegmatitic-hydrothermal system from the Mt. Capanne plutonic complex

prevents the formation of sulphide-arsenides, such as arsenopyrite. The extreme reducing conditions during the entrapment of fluids may result in the precipitation of native arsenic, and is consistent with the presence of H_2 in the vapour phase of fluid inclusions in tourmaline. A reduced fluid environment in the early magmatic-hydrothermal stage is interpreted from the presence of CH_4 - H_2 gas mixture and the absence of CO_2 in fluid inclusions in plagioclase and quartz from the leucogranite dykes

Andalusite stability and granite solidus

Andalusite and cordierite are primary phases in the leucogranite dykes and aplite-pegmatite dykes from Elba (Pezzotta 2000; Schilli 2015). The entrapment conditions of inclusions in andalusite in leucogranite (sample 67E) cannot be reconstructed from their fluid properties because the probable original H_2O -rich fluid has reacted with the host mineral to form step-daughter crystals quartz and diaspore. The concept of H_2O -loss due to the formation of step-daughter crystals was also described by Kleinfeld and Bakker (2002). The gas mixture in the remaining vapour phase is rich in CO_2 (low density) with minor amounts of CH_4 , H_2 and N_2 . The CH_4 and H_2 may evidence a minor input and mixing with an external reduced fluid. The hydrogen may also have entered fluid inclusions through diffusion.

Table 5 Composition of the aqueous liquid solution of fluid inclusions in tourmaline (sample 85A), graphically obtained in the ternary H_2O - NaCl - H_3BO_3 phase diagram (Fig. 11) from ice dissolution at the cotectic line and final dissolution of sassolite according to the data in Appendix F

Sample 85A tourmaline	Mass fractions liquid phase		
	H_2O	NaCl	H_3BO_3
fi1	0.849	0.105	0.046
fi2	0.861	0.098	0.043
fi3	0.853	0.109	0.038
fi4	0.859	0.101	0.040
fi5	0.861	0.100	0.039
fi6	0.858	0.100	0.042
fi7	0.833	0.120	0.047
fi9	0.887	0.073	0.040
fi11	0.854	0.096	0.050
fi15	0.872	0.100	0.028
fi16	0.860	0.097	0.043
fi17	0.862	0.098	0.040
fi20	0.858	0.115	0.027
fi26	0.858	0.092	0.050
fi27	0.859	0.092	0.049
fi30	0.862	0.088	0.050

Table 6 Calculated properties of vapour phase (composition and molar volume) and bulk fluid inclusion properties of fluid inclusions in quartz from sample 85A

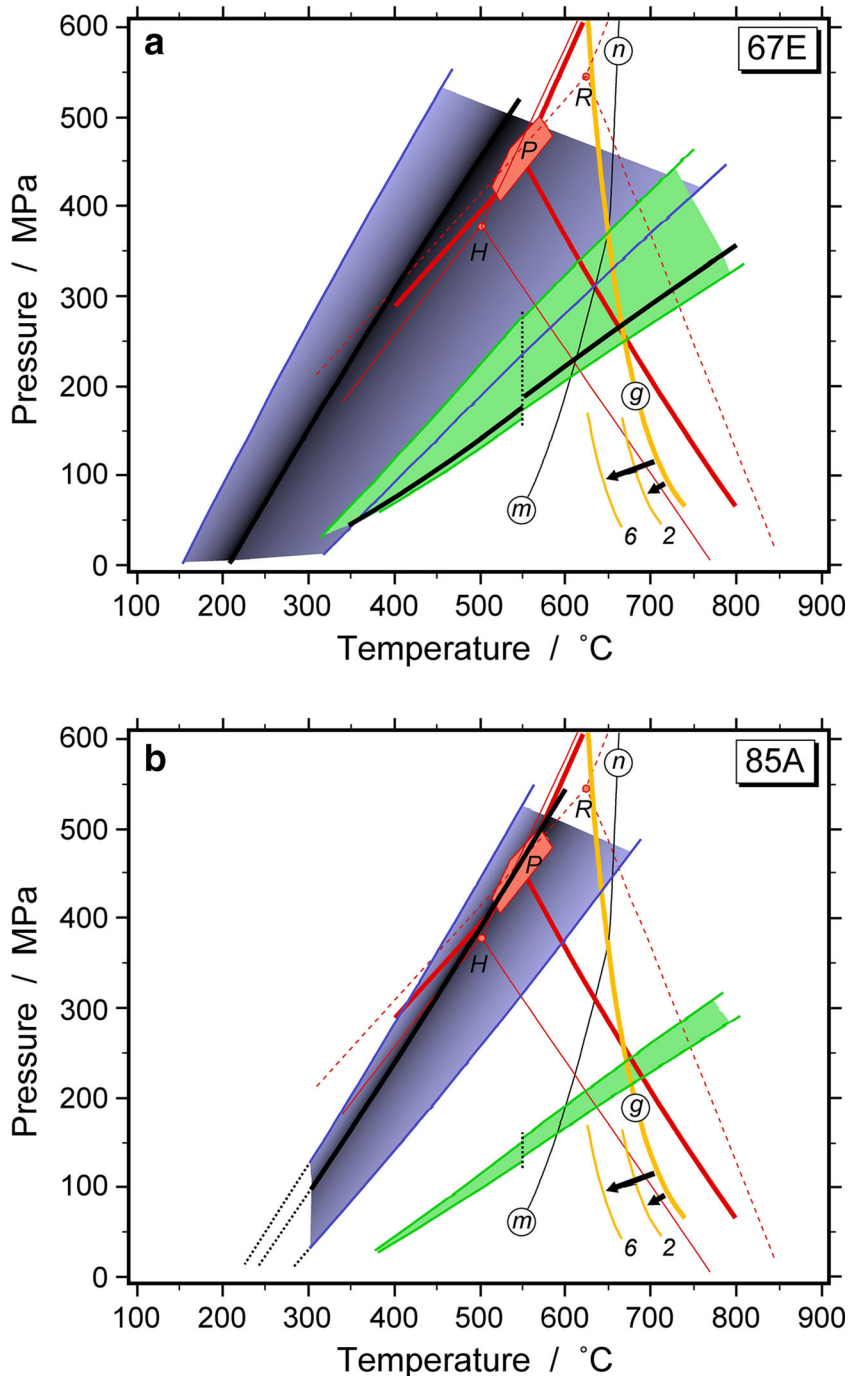
		Vapour phase			Bulk fluid inclusion				
		x(CO ₂)	x(CH ₄)	V _m cm ³ · mol ⁻¹	x(H ₂ O)	x(CO ₂)	x(CH ₄)	x(NaCl)	V _m cm ³ · mol ⁻¹
85A	fi8	0.982	0.018	2044	0.9787	0.0159	0.0001	0.0053	24.30
Qtz1	fi9	0.983	0.017	2129	0.9725	0.0146	0.0000	0.0128	22.71
	fi11	0.883	0.117	1937	0.9803	0.0142	0.0003	0.0052	22.50
	fi19	0.957	0.043	2116	0.9731	0.0143	0.0001	0.0124	22.69
	fi20	0.968	0.032	2157	0.9715	0.0141	0.0001	0.0144	22.20
	fi21	0.955	0.045	2064	0.9765	0.0145	0.0001	0.0089	22.34
	fi22	0.978	0.022	2103	0.9751	0.0150	0.0001	0.0099	23.20
	fi23	0.989	0.011	2093	0.9751	0.0165	0.0000	0.0083	26.07
	fi24	0.959	0.041	2097	0.9745	0.0145	0.0001	0.0109	22.66
	fi27	0.858	0.142	1931	0.9791	0.0138	0.0003	0.0068	22.26
	fi29	0.916	0.084	1910	0.9846	0.0146	0.0002	0.0006	21.88
85A	fi1	0.898	0.102	1978	0.9788	0.0139	0.0002	0.0071	21.76
Qtz2	fi3	0.883	0.117	1963	0.9788	0.0137	0.0003	0.0072	21.76
	fi4	0.927	0.073	2015	0.9780	0.0143	0.0002	0.0075	22.30
	fi6	0.903	0.097	2004	0.9767	0.0144	0.0003	0.0086	23.14
	fi7	0.925	0.075	2013	0.9776	0.0147	0.0002	0.0075	23.13
	fi8	0.927	0.073	2002	0.9789	0.0144	0.0002	0.0065	22.28
	fi9	0.942	0.058	2038	0.9771	0.0148	0.0002	0.0080	23.14
	fi12	0.972	0.028	2082	0.9759	0.0151	0.0001	0.0089	23.47
	fii13	0.775	0.225	1842	0.9789	0.0133	0.0007	0.0071	23.05
	fi16	0.941	0.059	2009	0.9793	0.0146	0.0001	0.0060	22.27
	fi21	0.979	0.021	2076	0.9774	0.0147	0.0000	0.0079	22.33
	fi24	0.983	0.017	2066	0.9780	0.0151	0.0000	0.0068	22.85
	fi26	0.979	0.021	2076	0.9773	0.0144	0.0000	0.0079	21.56
	fi27	0.956	0.044	2031	0.9790	0.0145	0.0001	0.0064	22.03
	fi30	0.976	0.024	2080	0.9770	0.0145	0.0001	0.0084	22.08
fi32	0.961	0.039	2085	0.9753	0.0147	0.0001	0.0099	22.91	
fi38	0.925	0.075	2006	0.9786	0.0142	0.0002	0.0070	21.87	
fi40	0.954	0.046	2043	0.9779	0.0146	0.0001	0.0074	22.14	

The andalusite-sillimanite equilibrium must cross the granite solidus resulting in an overlap of the andalusite stability fields and silicate melts in order to crystallize magmatic andalusite. The stability field of andalusite and cordierite in pegmatitic systems (peraluminous) is restricted to relative low pressures (e.g., Clarke et al. 2005, and reference therein). The Fe-content in pink-zoned andalusite from the studied leucogranite dykes (up to 2.68 mass% FeO, Electronic Appendix A) is much higher than illustrated by Clarke et al. (2005). Only few melt inclusion assemblages were reported by Clarke et al. (2005), and fluid inclusion assemblages were not described or observed in this review manuscript on the occurrence and origin of andalusite in peraluminous felsic igneous rock. The absence of melt inclusions in our studied euhedral andalusite crystals may exclude a magmatic origin, however, primary crystallization from a melt is evidenced by

textural relationships. The presence of abundant aqueous fluids (i.e., water-saturated system) must have favoured the formation of primary fluid inclusions, which were modified after entrapment. The formation of andalusite in leucogranite in the magmatic-hydrothermal stage of the Mt. Capanne pluton may occur in a very limited temperature-pressure window, where the upper-limit is defined by the andalusite-sillimanite equilibrium line and the lower-limit by the water-saturated granite solidus curve (Fig. 12). The uncertainty in the location of the andalusite-sillimanite equilibrium (Kerrick 1990, and references therein) allows a certain variation in formation conditions. The definition according to Holdaway and Mukhopadhyay (1993) does not allow an overlap between andalusite stability and solidus curve, which can only be obtained from the stability field estimations of Pattison (1992) or Richardson et al. (1969). The variability in the

location of the granite solidus is defined by the concentration of the solidus. In contrast, the presence of CO₂-CH₄-H₂ bear-

Fig. 12 Temperature-pressure phase diagram with isochores for the fluid inclusion assemblages in the leucogranite sample 67E (a) and aplite-pegmatite sample 85A (b). The yellow curved line (g) is the water saturated granite solidus (*albite + k-feldspar + quartz + H₂O = liquid*, e.g., Thompson and Tracy 1979), which is depressed to lower temperatures by specific boron contents (2 and 6 mass% B₂O₃, Pichavant 1981). The stability fields of Al₂SiO₅ polymorphs are illustrated with red-lines, H = Holdaway and Mukhopadhyay (1993); R = Richardson et al. (1969); and P = Pattison (1992). Line *m* is the muscovite breakdown reaction at relative low pressures: *muscovite + quartz = andalusite + k-feldspar + H₂O* (e.g., Thompson and Thompson 1976). Line *n* is the muscovite breakdown reaction at relative high pressures: *muscovite + quartz + plagioclase = sillimanite + k-feldspar + liquid* (e.g., Kerrick 1972). The green isochores in (a) are for Type 2 fluid inclusions, and the dark blue isochores are for Type 3 fluid inclusions in quartz from the leucogranite dyke. The included black isochores represents the mode values. The green isochores in (b) are for inclusions in tourmaline, and the dark blue isochors are for quartz from the aplite-pegmatite dykes. The dashed extensions are extrapolated isochores to lower temperatures



of B₂O₃ (e.g., Pichavant 1981) and the activity of water (e.g., Schmidt et al. 1997) in the melt. According to the partitioning of boron between melt and fluid phase in the hydrothermal stage of the development of a pegmatitic system (e.g., Pichavant 1981; Thomas et al. 2003), 4.2 amount % of H₃BO₃ (Table 5) in the fluid phase corresponds to similar concentrations in the melt, and a depression of about 40 °C

ing fluids reduces the water activity, which increases the solidus temperature in a haplogranitic system (e.g., Schmidt et al. 1997). However, all fluid inclusion assemblages are rich in H₂O and the concentration of carbon species do not exceeds 7 amount %. The low concentration of CO₂ is also reflected by the absence of accidentally trapped minerals such as dawsonite (c.f. Sirbescu and Nabelek 2003).

Fluid trapping conditions

Most of the described fluid inclusion assemblages in sample 67E (leucogranite dyke) and 85A (aplite-pegmatite dyke) are homogeneous. Consequently, fluid entrapment must have taken place at super-critical conditions along isochores, which must be constructed according to specific equations of state. Bakker (2003) has illustrated the existence of abundant equations of state in the software package *FLUIDS*. Selection of one equation depends on its accuracy, which can be obtained from comparison with experimental data of specific fluid systems, and considering temperature and pressure limits. In absence of experimental data, the equations can be compared to various unified Helmholtz energy functions for pure fluid end-members, e.g., Haar et al. (1984) for pure H₂O. These functions are the most accurate in reproducing a variety of *p-T-V* and other thermodynamic properties. Simplifications have to be taken into account if the measured fluid properties are highly complex and do not fit to the limitations of published equations of state.

Type 3 fluid inclusions in quartz from sample 67E are nearly pure H₂O, with only minor amounts of gases and salt (less than 1 amount %, see Table 4). Therefore, accurate isochores can be constructed with the program *Loner HGK* (Fig. 12a). The isochores of fluids that are trapped in *Type 2* inclusions in quartz from sample 67E, and in quartz and tourmaline from sample 85A can be calculated with equations of state for

quaternary H₂O-CO₂-CH₄-NaCl fluid systems (programs *Loner B* and *Loner AP*). Calculations are restricted to the program *Loner B* if additional gases such as H₂ and N₂ are included. Alternatively, these isochores can be calculated in a simplified binary H₂O-NaCl fluid system (e.g., *AqSo DH*), if the effect of the presence of gases on bulk fluid properties is neglected. *fi21* in quartz from sample 85A (*Qtz1*, Table 6) can be used to illustrate the test to determine the most accurate equation to calculate isochores (Table 7). This inclusion homogenizes at 245.1 °C into the liquid phase. In a pure H₂O fluid, this temperature corresponds to a molar volume of 22.34 cm³ · mol⁻¹ (*Loner HGK*), and the isochore reaches a pressure of 482.8 MPa at 600 °C. Higher concentrations of CO₂-CH₄ (*x*=0.0146) and NaCl (*x*=0.0089) in this fluid cause a significant shift of pure H₂O isochors at higher pressures and temperatures. *fi21* has an ice dissolution temperature of -3.2 °C that corresponds to *x*(NaCl)=0.01651 (*AqSo WNK*). The same homogenization temperature corresponds to a molar volume of 21.90 cm³ · mol⁻¹, and this isochore reaches higher pressures, 510 MPa at 600 °C (*AqSo DH*). The equation of state in *AqSo DH* for H₂O-NaCl mixtures includes per definitions the pure H₂O equation according to Haar et al. (1984). Complex bulk fluid properties calculated with the program *ICE* (Table 6) can be used to calculate the isochore of *fi21* in the quaternary H₂O-CO₂-CH₄-NaCl fluid system with *Loner B* and *Loner AP* (Table 7). However, these equations cannot be used to estimate accurately molar

Table 7 Calculated isochores with the programs *Loner HGK*, *AqSo DH*, *Loner B* and *Loner AP* for fluid inclusion *fi21* from *Qtz1* in sample 85A (see Table 6)

EoS	Loner HGK ^a	AqSo DH ^b	Loner B ^c		Loner AP ^d	
V _m	22.34 cm ³ · mol ⁻¹	21.90 cm ³ · mol ⁻¹	22.34 cm ³ · mol ⁻¹ *		22.34 cm ³ · mol ⁻¹ *	
Temperature (°C)	Pressure (MPa)					
300	79.6	81.5	50.3	31.2 (-60.8 %)	88.4	72.3 (-9.2 %)
350	149.7	153.9	131.5	113.9 (-23.9 %)	154.8	136.6 (-8.8 %)
400	219.3	226.9	208.7	191.7 (-12.6 %)	223.2	203.9 (-7.0 %)
450	287.7	299.6	283.0	265.8 (-7.6 %)	294.8	273.9 (-4.8 %)
500	354.6	371.3	354.9	337.4 (-4.9 %)	369.4	346.3 (-2.3 %)
550	419.7	441.5	424.9	406.9 (-3.0 %)	445.9	420.7 (+0.2 %)
600	482.8	510.0	493.3	474.9 (-1.6 %)	523.4	496.7 (+2.9 %)
650	544.1	576.6	560.4	541.5 (-0.5 %)	602.4	574.2 (+5.5 %)
700	603.6	641.3	626.4	607.1 (+0.6 %)	682.9	652.8 (+8.2 %)

EoS is equation of state; *V_m* is molar volume. The numbers in bold are extrapolated beyond the limits of the equation of state (500 MPa). The numbers in *italic* are the pure H₂O end-member isochores from *Loner B* and *Loner AP*. The numbers in *brackets* are the corresponding deviation (in %)

^a pure H₂O, Haar et al. (1984)

^b binary H₂O-NaCl, Driesner (2007)

^c quaternary H₂O-CO₂-CH₄-NaCl, Bakker (1999)

^d quaternary H₂O-CO₂-CH₄-NaCl, Anderko and Pitzer (1993), Duan et al. (1995, 2003)

*homogenization temperature cannot be used to calculate bulk molar volume with this equation of state, therefore, the value of *fi21* in Table 6 is selected

volumes directly from T_h below 300 °C. The pure H₂O fluid end-member of these equations of state is compared to the isochore of pure H₂O calculated with *Loner HGK* (Table 7). *Loner B* is highly inaccurate below 500 °C, but is within 5 % deviation at higher temperatures and pressures, whereas *Loner AP* is only reliable in the range 450–600 °C, and result in highly overestimated pressures at higher temperatures, and up to 10 % deviation at lower temperatures. Therefore, fluid trapping conditions with the quaternary H₂O–CO₂–CH₄–NaCl system of the Monte Capanne plutonic system that exceed 550 °C are best modelled with *Loner B*, whereas *Loner AP* is suitable to model this fluid system below 550 °C (Fig. 12).

The inferred trapping conditions of *Type 2* fluid inclusions in quartz from leucogranite dykes range from 670 °C and 270 MPa to 720 °C and 310 MPa (Fig. 12a). Subsequently, fluids are continuously trapped in quartz during further cooling and exhumation of the rock, down to around 200 °C and 50 MPa. Trapping conditions of fluids in tourmaline from aplite-pegmatite veins occurred at lower pressures, ranging from 680 °C and 230 MPa to 740 °C and 270 MPa (Fig. 12b). The quartz in the aplite-pegmatite dykes record a distinct trapping event at much lower temperatures and pressures, at about 250 to 300 °C and 50 to 100 MPa.

Comparison with previous fluid inclusion studies

Ruggieri and Lattanzi (1992) examined fluid inclusions in quartz, beryl and tourmaline from miarolitic cavities, and in quartz from massive pegmatites from the eastern Mt. Capanne plutonic complex. Although they have described similar low salinity H₂O-rich fluid types, there are some important new details, results and differences in fluid property estimations that allow an improved interpretation of trapping conditions and environment of crystallization of leucogranite and aplite-pegmatite dykes. The new results include more detailed analyses of the gas composition of the vapour phase in different fluid inclusion assemblages, that is clearly distinct from previous analyses: the mixture (Fig. 2) includes H₂ and higher concentrations of CH₄, N₂, and only trace of H₂S in some inclusions. Moreover, the presence of arsenic and H₃BO₃ as daughter crystal and dissolved in the aqueous solution was not described by Ruggieri and Lattanzi (1992). They estimated bulk fluid properties from unspecified assumptions about volume fractions of vapour-liquid phases, neglecting the solubility of gases, and selecting a general average density of a pure CO₂ vapour phase, whereas clathrate dissolution temperatures were not used, or not observed. This CO₂ density is usually underestimated due to restricted visibility for LV → V homogenization. Uncertainties analyses of calculated isochores were not performed by Ruggieri and Lattanzi (1992).

Petalite (LiAlSi₄O₁₀) and quartz is described as a stable assemblage in some pegmatitic vugs of Elba (e.g., Pezzotta

2000). Although Li-bearing minerals were not identified in Ruggieri and Lattanzi (1992), the stability of petalite in the eukryptite-quartz-water system was used to estimate the upper and lower limits of trapping conditions of fluids. A not further specified assumption of trapping pressures (150 MPa) results in trapping temperatures of primary inclusions in quartz and tourmaline at 475 to 580 °C, which is well below the possibilities to crystallize magmatic andalusite, and inconsistent with our results.

Rossetti and Tecce (2008) have described a highly saline fluid (up to 70 eq. mass% NaCl) in skarn minerals (grossular-andradite, vesuvianite, and quartz) that developed in the thermal aureole of the north-eastern part of the Mt. Capanne plutonic complex. This skarn developed in the contact zone to marbles and calcschists of the tectonic unit Complex IV (Dini et al. 2002). Our fluid inclusion studies in the leucogranite and aplite-pegmatite dykes that are located within the same thermal aureole, but within serpentinites do not reveal any evidence of the presence of a highly saline brine, and NaCl is only present in minor amounts. It is therefore unlikely that the magmatic-hydrothermal system of the Mt. Capanne pluton is the source of a hypersaline brine in the skarn. Both studies reveal the existence of a reduced fluid, i.e., CH₄ dominated, in the thermal aureole in metasediments. Therefore marbles, calcschists and serpentinites must have produced a highly reducing fluid during contact metamorphism. Rossetti and

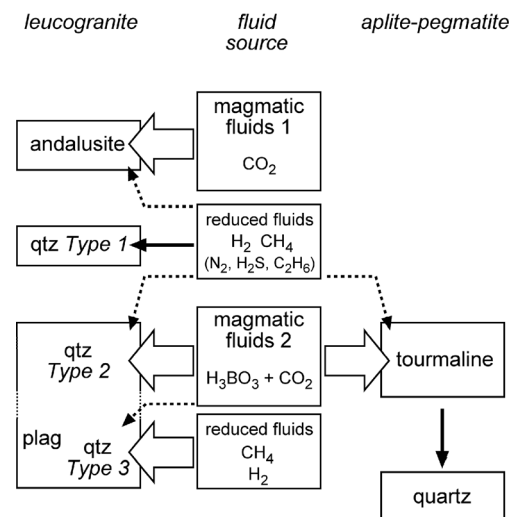


Fig. 13 Schematic diagram to illustrate the relationship between fluid sources and fluid inclusion assemblages that are analysed in leucogranite dykes and aplite-pegmatite dykes. Relative timing of crystallization and fluid entrapment is illustrated by the vertical order of boxes (from top to bottom). All fluid systems are highly enriched in H₂O with only traces of NaCl, CO₂, CH₄, H₂ and other gases (up to 7 mass%). The *large arrows* indicate the main type of fluid that is entrapped in a specific mineral, whereas the *small dashed arrows* indicated the entrapment of minor amounts of an additional fluid. The *vertical arrow* from tourmaline to quartz in the aplite-pegmatite dyke illustrates that both minerals evolved from the second magmatic fluid, quartz after tourmaline, without the input of a second reduced metamorphic fluid. See text for further details

Tecce (2008) suggest that original CO₂-rich fluids in the marbles and calcschists were reduced by the gain of hydrogen that was obtained by the change in oxygen fugacity from an infiltrating Fe-rich brine. Nevertheless, because this skarn has entrapped a CH₄-dominant metamorphic fluid, it is unlikely that CO₂ entrapped in leucogranite and aplite-pegmatite dykes of the Mt. Capanne complex originate from this metamorphic source. Serpentinities are unlike to contain original CO₂-rich metamorphic fluids, therefore CO₂ can be assigned to a magmatic origin in our studied samples, similar to the observations of Ruggieri and Lattanzi (1992).

Fluid evolution

Figure 13 illustrates schematically the interpreted fluid events and compositional changes during entrapment of fluid inclusion assemblages in leucogranite dykes and aplite-pegmatite dykes from the late magmatic-hydrothermal stage of the Mt. Capanne plutonic complex. The fluid inclusion assemblages record multiple pulses of H₂O-rich, NaCl-poor magmatic and reduced metamorphic fluid stages. The occurrence of a low salinity aqueous liquid with minor amounts of CO₂ in fluid inclusions in pegmatites was also described by London (2008, and references therein). The fingerprint of these magmatic fluids in andalusite in leucogranite dykes is suggested to be the CO₂-rich gas mixture, whereas the H₂O was completely lost due to post-entrapment modifications. The presence of small amounts of CH₄, H₂ and N₂ illustrates that reduced fluids from the serpentinites were already injected in this early stage. This reduced fluid completely replaced the magmatic fluid during the development of *Type 1* primary inclusions in quartz, still in the presence of abundant suspended mica crystals from the magmatic fluid. Subsequently, a second major magmatic pulse introduces a boron-rich fluid during the emplacement of aplite-pegmatite dykes that mixes with the remaining reduced fluid, and produces variable CO₂-CH₄ gas mixture. This fluid also includes other gas components, such as H₂, N₂, H₂S, and C₂H₆ that may origin from the input of more reduced fluids from the serpentinites. This fluid is trapped in quartz from the leucogranite (*Type 2*) and represents the first crystallization conditions of tourmaline in aplite-pegmatites. The isochore interpretation illustrates that this fluid was trapped at lower pressures than in leucogranites. Reduced fluids are the major fluid source in the late stage of the development of leucogranite dykes, resulting in CH₄-H₂ gas mixtures that are trapped in quartz (*Type 3*) and plagioclase. The aplite-pegmatite is not affected by this injection of reduced fluids and records only a late stage fluid entrapment in quartz from the remnants of the original magmatic fluid source, still containing a CO₂-rich gas mixture and some boron.

Acknowledgments Comments of Peter Nabelek and an anonymous reviewer were helpful to improve the quality of this manuscript. Federica Zaccarini is thanked for her assistance on the electron microprobe, and Helmut Mühlhans for the preparation of thin and thick-sections.

References

- Anderko A, Pitzer KS (1993) Equation-of-state representation of phase equilibria and volumetric properties of the system NaCl-H₂O above 573 K. *Geochim Cosmochim Acta* 57:1657–1680
- Anderson AJ, McCarron T (2011) Three-dimensional textural and chemical characterization of polyphase inclusions in spodumene using a dual focussed ion beam - scanning electron microprobe (FIB-SEM). *Can Mineral* 49:541–553
- Auricchio C, Ottolini L, Pezzotta F (1999) Electron- and ion-microprobe analyses, and genetic inferences of tourmalines of the foitite-schorl solid solution, Elba Island (Italy). *Eur J Mineral* 11: 217–225
- Auricchio C, Conte AM, de Vito C, Ottolini L (2012) Beryl from miarolitic pockets of granitic pegmatites, Elba, Italy: characterization of crystal chemistry by means of EMP and SIMS analyses. *Can Mineral* 50:1467–1488
- Bakker RJ (1997) *CLATHRATES*: computer programs to calculate fluid inclusion V-X properties using clathrate melting temperatures. *Comput Geosci* 23:1–18
- Bakker RJ (1998) Improvements in clathrate modelling: II. the H₂O-CO₂-CH₄-N₂-C₂H₆ fluid system. In: Henriot JP, Mienert J (eds) Gas hydrates: relevance to world margin stability and climate change. *Geol Soc London Spec Publ* 137:75–105
- Bakker RJ (1999) Adaptation of the Bowers and Helgeson (1983) equation of state to the H₂O-CO₂-CH₄-N₂-NaCl system. *Chem Geol* 154:225–236
- Bakker RJ (2003) Package *FLUIDS* 1. Computer programs for the analysis of fluid inclusion data and for modelling bulk fluid properties. *Chem Geol* 194:3–23
- Bakker RJ (2004) Raman spectra of fluid and crystal mixtures in the systems H₂O, H₂O-NaCl and H₂O-MgCl₂ at low temperatures: application to fluid inclusion research. *Can Mineral* 42:1283–1314
- Bakker RJ (2011) The use of quantities, units and symbols in fluid inclusion research. *Ber Geol Bundesanst* 87:5–11
- Bakker RJ (2012) Package *Fluids*. Part 4: thermodynamic modelling and purely empirical equations for H₂O-NaCl-KCl solutions. *Mineral Petrol* 105:1–29
- Bakker RJ, Diamond LW (2006) Estimation of volume fractions of liquid and vapor phases in fluid inclusions, and definition of inclusions shape. *Am Mineral* 91:635–657
- Bakker RJ, Dubessy J, Cathelineau M (1996) Improvements in clathrate modelling: I. the H₂O-CO₂ system with various salts. *Geochim Cosmochim Acta* 60:1657–1681
- Baumgartner M, Bakker RJ (2009) Raman spectroscopy of pure H₂O and NaCl-H₂O containing synthetic fluid inclusions in quartz - a study of polarization effects. *Mineral Petrol* 95:1–15
- Baumgartner M, Bakker RJ (2010) Raman spectra of ice and salt hydrates in synthetic fluid inclusions. *Chem Geol* 275:58–66
- Benvenuti M, Bortolotti V, Conticelli S, Pandelli E, Principi G (2001) 2 - Elba Island. A: introduction. *Ofoliti* 26:321–330
- Borisova AY, Pokrovsky GS, Pichavant M, Freyrier R, Candaudap F (2010) Arsenic enrichment in hydrous peraluminous melts: insights from femtosecond laser ablation-inductively coupled plasma-quadrupole mass spectrometry, and in situ X-ray absorption fine structure spectroscopy. *Am Mineral* 95:1095–2010
- Bortolotti V, Fazzuoli M, Paudeli E, Principi G, Babbini A, Corti S (2001) Geology of central and eastern Elba Island, Italy. *Ofoliti* 26:97–150

- Burke EAJ (2001) Raman microspectrometry of fluid inclusions. *Lithos* 55:139–158
- Clark CM (2007) Tourmaline: structural formula calculations. *Can Mineral* 45:229–237
- Clarke DB, Dorais M, Barbarin B, Barker D, Cesare B, Clarke G, el Baghdadi M, Erdmann S, Förster H-J, Gaete M, Gottesmann B, Jamieson RA, Kontak DJ, Koller F, Leal Gomes C, London D, Morgan GB, Neves LJP, Pattison DRM, Pereira AJSC, Pichavant M, Rapela CW, Renno AD, Richards S, Roberts M, Rottura A, Saavedra J, Nobrega Sial A, Toselli AJ, Ugidos JM, Uher P, Villaseca C, Visona D, Whitney DL, Williamson B, Woodard HH (2005) Occurrence and origin of andalusite in peraluminous felsic igneous rocks. *J Petrol* 46:441–472
- Dini A, Innocenti F, Rocchi S, Tonarini S, Westerman DS (2002) The magmatic evolution of the late Miocene laccolith-pluton-dyke granitic complex of Elba Island, Italy. *Geol Mag* 139:257–279
- Dini A, Rocchi S, Westerman DS (2004) Reaction microtextures of REE-Y-Th-U accessory minerals in the Monte Capanne pluton (Elba Island, Italy): a possible indicator of hybridization processes. *Lithos* 78:101–118
- Doppler G, Bakker RJ, Baumgartner M (2013) Fluid inclusion modification by H₂O and D₂O diffusion: the influence of inclusion depth, size and shape in re-equilibration experiments. *Contrib Mineral Petrol* 165:1259–1274
- Driesner T (2007) The system H₂O-NaCl. Part II. Correlations for molar volume, enthalpy, and isobaric heat capacity from 0 to 1000 °C, 1 to 5000 bar, and 0 to 1 xNaCl. *Geochim Cosmochim Acta* 71:4902–4919
- Driesner T, Heinrich CA (2007) The system H₂O-NaCl. Part I: correlation formulae for phase relations in the temperature-pressure-composition space from 0 to 1000 °C, 0 to 5000 bar, and 0 to 1 xNaCl. *Geochim Cosmochim Acta* 71:4880–4901
- Duan Z, Möller N, Weare JH (1992) An equation of state for the CH₄-CO₂-H₂O system: II. mixtures from 50 to 1000 °C and 0 to 1000 bar. *Geochim Cosmochim Acta* 56:2619–2631
- Duan Z, Möller N, Weare JH (1995) Equation of state for the NaCl-H₂O-CO₂ system: prediction of phase equilibria and volumetric properties. *Geochim Cosmochim Acta* 59:2869–2882
- Duan Z, Möller N, Weare JH (2003) Equation of state for the NaCl-H₂O-CH₄ system and the NaCl-H₂O-CO₂-CH₄ system: phase equilibria and volumetric properties above 573 K. *Geochim Cosmochim Acta* 67:671–680
- Haar L, Gallagher JS, Kell GS (1984) NBS/NRC steam tables. Hemisphere Publishing Corporation, Washington DC
- Hawthorne FC, Henry DJ (1999) Classification of the minerals of the tourmaline group. *Eur J Mineral* 11:201–215
- Hemley JJ, Montoya JW, Marinenko JW, Luce RW (1980) Equilibria in the system Al₂O₃-SiO₂-H₂O and some general implications for alteration/mineralization processes. *Econ Geol* 75:210–228
- Holdaway MJ, Mukhopadhyay B (1993) A re-evaluation of the stability relations of andalusite: thermochemical data and phase diagram for the aluminium silicates. *Am Mineral* 78:298–315
- Innocenti F, Serri G, Ferrara G, Manetti P, Tonarini S (1992) Genesis and classification of the rocks of the Tuscan Magmatic Province: thirty years after Marinelli's model. *Acta Vulcanol* 2:247–265
- James-Smith J, Cauzid J, Testemale D, Liu W, Hazemann J-L, Proux O, Etschmann B, Philippot P, Banks D, Williams P, Brugger J (2010) Arsenic speciation in fluid inclusions using micro-beam X-ray absorption spectroscopy. *Am Mineral* 95:921–932
- Janda R, Heller G (1979) Ramanspektroskopische Untersuchungen an festen und in Wasser gelösten Polyboraten. *Z Naturforsch* 34b: 585–590
- Kerrick DM (1972) Experimental determination of muscovite + quartz stability with PH₂O < Ptotal. *Am J Sci* 272:946–958
- Kerrick DM (1990) The Al₂SiO₅ polymorphs. *Rev Mineral* 22:406
- Kleinfeld B, Bakker RJ (2002) Fluid inclusions as microchemical systems: evidence and modelling of fluid host interactions in plagioclase. *J Metamorph Geol* 26:845–858
- London D (2008) Pegmatites. *Can Mineral, Spec Publ* 10:347
- Mernagh TP, Wilde AR (1989) The use of the Raman microprobe for the determination of salinity in fluid inclusions. *Geochim Cosmochim Acta* 53:765–771
- Pattison DRM (1992) Stability of andalusite and sillimanite and the Al₂SiO₅ triple point: constraints from the Ballachulish aureole, Scotland. *J Geol* 100:423–446
- Peng DY, Robinson DB (1976) A new two constant equation of state. *Ind Eng Chem Fundam* 15:59–64
- Peretyazhko IS (2009) Inclusions of magmatic fluids: P-V-T-X properties of aqueous salt solutions of various types and petrological implications. *Petrology* 17:197–221
- Peretyazhko IS, Zagorsky VE (2002) The influence of H₃BO₃ on fluid pressure in granitic pegmatite miaroles: a computation of isochores and the density of boric acid solutions. *Dokl Earth Sci* 383A:340–345
- Peretyazhko IS, Prokorev VY, Zagorskii VE, Smirnov SZ (2000) Role of boric acid in the formation of pegmatitic and hydrothermal minerals: petrologic consequences of sassolite (H₃BO₃) discovery in fluid inclusions. *Petrology* 8:214–237
- Pezzotta F (2000) Internal structures, parageneses and classification of the miarolitic Li-bearing complex pegmatites of Elba Island (Italy). *Mem Soc Ital Sci Nat Mus Civ Sto Nat Milano* 30:29–43
- Pichavant M (1981) An experimental study of the effect of boron on a water saturated haplogranite at 1 kbar vapour pressure. *Contrib Mineral Petrol* 76:430–439
- Pitzer KS (1991) Ion interaction approach: theory and data correlation. In: Pitzer KS (ed) Activity coefficient in electrolyte solutions. CRC Press, Boca Raton, pp 76–153
- Pokrovski G, Gout R, Schott J, Zotov A, Harrichoury J-C (1996) Thermodynamic properties and stoichiometry of As(III) hydroxide complexes at hydrothermal conditions. *Geochim Cosmochim Acta* 60:737–749
- Richardson W, Gilbert MC, Bell PM (1969) Experimental determination of kyanite-andalusite and andalusite-sillimanite equilibria: the aluminium silicate triple point. *Am J Sci* 267:259–272
- Rickers K, Thomas R, Heinrich W (2006) The behavior of trace elements during the chemical evolution of the H₂O-, B-, and F-rich granite-pegmatite-hydrothermal system at Ehrenfriedersdorf, Germany: a SXRF study of melt and fluid inclusions. *Mineral Deposita* 41: 229–245
- Rossetti F, Tecce F (2008) Composition and evolution of fluids during skarn development in the Monte Capanne thermal aureole, Elba Island, central Italy. *Geofluids* 8:167–180
- Ruggieri G, Lattanzi P (1992) Fluid inclusion studies on Mt. Capanne pegmatites, Isola d'Elba, Tuscany, Italy. *Eur J Mineral* 4:1085–1096
- Schilli SE (2015) Mineralogical characterisation, fluid inclusions and formation conditions of aplite, pegmatite and quartz-tourmaline rich veins, Elba (Italy). Master Thesis, Montanuniversitaet Leoben (Austria)
- Schmidt BH, Holtz F, Scaillet B, Pichavant M (1997) The influence of H₂O-H₂ fluids and redox conditions on melting temperatures in the haplogranite system. *Contrib Mineral Petrol* 126:386–400
- Shepherd T, Rankin AH, Alderton DHM (1985) A practical guide to fluid inclusion studies. Blackie, Glasgow, p 239
- Sirbescu M-LC, Nabelek PI (2003) Dawsonite: an inclusion mineral in quartz from the Tin Mountain pegmatite, Black Hills, South Dakota. *Am Mineral* 88:1055–1060
- Sirbescu M-LC, Krukowski EG, Schmidt C, Thomas R, Samson IA, Bodnar RJ (2013) Analysis of boron in fluid inclusions by microthermometry, laser ablation ICP-MS, and Raman spectroscopy: application to the Cryo-Genie pegmatite, San Diego County, California, USA. *Chem Geol* 342:138–150

- Struzhkin VV, Militzer B, Mao WL, Mao H-K, Hemley RJ (2007) Hydrogen storage in molecular clathrates. *Chem Rev* 107:4133–4151
- Thomas R (2002) Determination of the H_3BO_3 concentration in fluid and melt inclusions in granite pegmatites by laser Raman microprobe spectroscopy. *Am Mineral* 87:56–68
- Thomas R, Förster H-J, Heinrich W (2003) The behaviour of boron in a peraluminous granite-pegmatite system and associated hydrothermal solutions: a melt and fluid-inclusion study. *Contrib Mineral Petrol* 144:457–472
- Thompson JB, Thompson AB (1976) A model system for mineral facies in pelitic schist. *Contrib Mineral Petrol* 58:243–277
- Thompson AB, Tracy RJ (1979) Model systems for anatexis of pelitic rocks II. Facies series melting and reactions in the system $\text{CaO-KAlO}_2\text{-NaAlO}_2\text{-Al}_2\text{O}_3\text{-SiO}_2\text{-H}_2\text{O}$. *Contrib Mineral Petrol* 70:429–438
- Wang P, Kosinski JJ, Lencka MM, Anderko A, Springer R (2013) Thermodynamic modelling of boric acid and selected metal borate systems. *Pure Appl Chem* 85:2117–2144
- Westerman DS, Dini A, Innocenti F, Rocchi S (2004a) When and where did hybridization occur? The case of the Monte Capanne Pluton, Italy. *Atl Geol* 39:147–162
- Westerman DS, Dini A, Innocenti F, Rocchi S (2004b) Rise and fall of a nested Christmas-tree laccolith complex, Elba Island, Italy. In: Breikreuz C, Petford N (eds) *Physical geology of high-level magmatic systems*. *Geol Soc London Spec Publ* 234:195–213

Appendix A

Electron-microprobe analyses and calculated cation content of andalusite (core and rim) from sample 67E.

	rim 1	rim 2	rim 3	core 1	core 2	core 3	core 4	core 5
<i>mass% of oxides measured and calculated with EMP</i>								
Al ₂ O ₃	61.51	61.51	61.55	60.86	61.24	61.18	60.88	60.49
SiO ₂	36.11	36.31	36.25	36.55	36.33	36.84	36.16	36.69
FeO	1.77	1.84	1.89	1.98	2.02	2.25	2.66	2.68
MgO	0.03	0.04	0.03	0.04	0.03	0.05	0.05	0.04
MnO	0.00	0.00	0.00	0.00	0.02	0.00	0.00	0.01
TiO ₂	0.04	0.08	0.04	0.07	0.08	0.11	0.10	0.04
Na ₂ O	0.00	0.03	0.00	0.02	0.00	0.01	0.02	0.01
CaO	0.00	0.00	0.00	0.02	0.00	0.01	0.00	0.02
K ₂ O	0.02	0.01	0.01	0.01	0.02	0.00	0.01	0.00
total	99.48	99.81	99.77	99.54	99.74	100.45	99.86	99.97
<i>numbers of cations based on twenty O</i>								
Al	7.942	7.918	7.928	7.859	7.897	7.839	7.867	7.805
Si	3.956	3.966	3.962	4.004	3.975	4.005	3.965	4.016
Fe ²⁺	0.162	0.168	0.173	0.182	0.185	0.205	0.244	0.245
Mg	0.005	0.006	0.004	0.007	0.004	0.007	0.008	0.006
Mn	-	-	-	-	0.001	-	-	0.001
Ti	0.003	0.007	0.003	0.005	0.007	0.009	0.008	0.003
Na	-	0.006	-	0.004	-	0.002	0.004	0.002
Ca	-	-	-	0.002	-	0.001	-	0.003
K	0.003	0.001	0.001	0.002	0.002	-	0.001	-

Appendix B

Electron-microprobe analyses and calculated cation content of rutile from sample 67E

	grain 1	grain 2	grain 3	grain 4	grain 5	grain 6
	<i>mass% of oxides measured and calculated with EMP</i>					
TiO ₂	74.09	73.20	73.79	73.36	73.87	75.34
Al ₂ O ₃	0.27	0.24	0.22	0.21	0.25	0.18
FeO	10.75	11.55	11.49	11.10	10.85	10.21
MnO	0.20	0.16	0.18	0.22	0.17	0.15
Cr ₂ O ₃	0.01	0.01	0.06	0.01	0.00	0.01
SnO ₂	4.29	4.30	4.07	4.34	4.12	4.09
WO ₃	0.30	0.30	0.27	0.45	0.48	0.31
Nb ₂ O ₅	6.30	6.51	6.98	6.62	6.83	6.03
Ta ₂ O ₅	3.90	3.47	3.42	3.46	2.62	3.21
ZrO ₂	0.06	0.08	0.04	0.09	0.05	0.08
total	100.17	99.82	100.51	99.84	99.24	99.60
	<i>number of cations on the basis of two O</i>					
Ti	0.828	0.823	0.823	0.824	0.829	0.840
Al	0.005	0.004	0.004	0.004	0.004	0.003
Fe ²⁺	0.134	0.144	0.142	0.139	0.136	0.127
Mn	0.003	0.002	0.002	0.003	0.002	0.002
Cr	0.000	0.000	0.001	0.000	0.000	0.001
Sn	0.025	0.026	0.024	0.026	0.025	0.024
W	0.001	0.001	0.001	0.002	0.002	0.001
Nb	0.042	0.044	0.047	0.045	0.046	0.040
Ta	0.016	0.014	0.014	0.014	0.011	0.013
Zr	0.001	0.001	0.000	0.001	0.000	0.001

Appendix C

Electron-microprobe analyses and calculated cation content of tourmaline (core and rim) from sample 85A

		core 1	core 2	core 3	core 4	core 5	rim 1	rim 2	rim 3	rim 4	rim 5	rim 6	rim 7
		<i>mass% of oxides measured and calculated by EMP</i>											
	Na ₂ O	1.36	1.38	1.41	1.48	1.48	1.67	1.67	1.71	1.72	1.74	1.77	1.79
	CaO	0.07	0.07	0.06	0.14	0.11	0.20	0.21	0.19	0.16	0.23	0.21	0.24
	FeO	9.63	9.96	9.81	9.81	9.65	10.81	10.67	11.26	11.04	10.86	11.00	10.22
	K ₂ O	0.03	0.03	0.02	0.04	0.03	0.04	0.03	0.04	0.03	0.04	0.04	0.04
	B ₂ O ₃	11.06	12.18	12.08	10.14	10.01	12.34	12.54	9.79	11.95	11.82	12.57	12.03
	MgO	1.93	1.95	1.90	1.97	1.93	2.03	1.95	1.96	1.73	1.94	1.90	3.06
	SiO ₂	35.52	36.32	35.20	35.77	35.16	34.88	33.71	34.36	34.70	34.29	33.57	34.85
	TiO ₂	0.27	0.27	0.34	0.46	0.42	0.90	0.73	0.82	0.69	0.74	0.74	0.65
	Al ₂ O ₃	35.58	35.68	34.79	36.60	36.65	34.98	34.44	34.69	65.40	64.40	35.50	33.95
	MnO	0.13	0.16	0.17	0.15	0.12	0.11	0.15	0.14	0.17	0.14	0.19	0.10
	F	0	0	0	0	0	0	0	0	0	0	0	0
	total	95.58	98.00	95.76	96.55	95.57	97.95	96.08	94.92	97.59	96.20	97.48	96.91
		<i>numbers of ions on the basis of thirty-one O, and a stoichiometric content of 4 apfu OH</i>											
X	□	0.545	0.553	0.534	0.494	0.495	0.433	0.422	0.393	0.421	0.392	0.394	0.382
	Na	0.435	0.428	0.451	0.473	0.479	0.525	0.535	0.564	0.543	0.558	0.561	0.567
	Ca	0.013	0.013	0.010	0.025	0.020	0.035	0.037	0.035	0.029	0.041	0.037	0.042
	K	0.007	0.006	0.005	0.008	0.006	0.007	0.006	0.008	0.007	0.009	0.008	0.009
Y ₃	Mg	0.475	0.467	0.466	0.483	0.479	0.489	0.480	0.495	0.421	0.478	0.461	0.746
	Fe ²⁺	1.331	1.338	1.349	1.352	1.342	1.466	1.473	1.594	1.506	1.503	1.501	1.400
	Mn	0.018	0.022	0.023	0.021	0.017	0.015	0.021	0.020	0.024	0.019	0.026	0.014
	Al	0.932	0.758	0.745	0.997	1.037	0.683	0.701	0.767	0.806	0.713	0.827	0.554
	Ti	0.033	0.032	0.041	0.057	0.053	0.110	0.090	0.104	0.084	0.093	0.091	0.080
Z ₆	Al	6.000	6.000	6.000	6.000	6.000	6.000	6.000	6.000	6.000	6.000	6.000	6.000
T ₆	Si	5.871	5.836	5.790	5.892	5.850	5.654	5.564	5.830	5.661	5.677	5.479	5.708
	Al	-	-	-	0.108	0.150	-	-	0.170	-	-	-	-
	B	0.129	0.164	0.210	-	-	0.346	0.436	-	0.339	0.323	0.521	0.292
B ₃	B	3.032	3.215	3.219	2.884	2.876	3.106	3.136	2.866	3.026	3.055	3.019	3.109
V ₃	OH*	3.000	3.000	3.000	3.000	3.000	3.000	3.000	3.000	3.000	3.000	3.000	3.000
W	OH*	1.000	1.000	1.000	1.000	1.000	1.000	1.000	1.000	1.000	1.000	1.000	1.000
	Mg #	0.263	0.259	0.257	0.263	0.263	0.250	0.246	0.237	0.219	0.241	0.235	0.348
	□ #	0.552	0.560	0.539	0.507	0.506	0.449	0.439	0.408	0.435	0.409	0.409	0.399

Mg # = Mg / (Mg + Fe)

□ = vacancy, defined as (1.0 - Na - Ca - K)

□ # = □ / (□ + Na + K)

OH* = assuming 4 apfu OH

Sample 67E, Type 2 Fluid Inclusions Quartz

	Microthermometry					Area Raman Peaks					extra Raman peaks in vapour in cm ⁻¹	Volume area fraction (vap)
	T _n (1) in °C	T _n (2) in °C	T _m (ice) in °C	T _m (cla) in °C	T _n (LV→L) in °C	CO ₂ 1283 cm ⁻¹	CO ₂ 1385 cm ⁻¹	CH ₄ 2914 cm ⁻¹	H ₂ 4152 cm ⁻¹	N ₂ * 2331 cm ⁻¹		
fi1	-29.1	-38	-6.9	+5.5	365.0	43827	72169	58380	1256	1260		0.44
fi3	-31.5			+1.4	370.8	5886	9800	15604	940	300		0.42
fi4	-28	-39	-6.5	+6.6	371.9	47216	73530	96472	12500	1975	3013, 3065	0.43
fi5	-37	-46	-6.9	+6.6	365.2	6705	8877	90555	354	600		0.33
fi6	-29	-39	-6.2		377.2	14738	25355	93232	3889	534		0.43
fi7	-29	-38	-6.0	+7.5	381.3	9695	14254	52904	873	400		0.44
fi8	-29	-40	-6.2	+6.1	378.2	19852	34434	57467	1732	600		0.43
fi9	-28	-38	-7.2	+6.8	370.9	25887	42525	59479	1907	500		0.37
fi19	-31	-36	-3.7	+11.3	323.7	5622	10499	248739	4750	700		0.31
fi21	-33		-2.4		352.3	2387	3310	97382	5872	600		0.37
fi22	-32		-1.4	+5.5	367.7	<i>no Raman analyses</i>					irreg.	
fi34	-30	-41	-7.6	+5.7	363.4	25278	37672	17685	1178	1124		0.35
fi35	-36		-4.0	+6.0	372.8	<i>no Raman analyses</i>					0.41	
fi37	-30	-39	-7.7	+7.3	365.7	24570	35897	17605	1370	1460		0.43
fi38	-27	-37	-7.2	+6.6	369.6	<i>no Raman analyses</i>					irreg.	
fi39	-33		-2.4		358.1	9673	15509	83766	6670	906	3012, 3061	0.40
fi41	-26.5	-37	-5.7	+6.5	366.8	<i>no Raman analyses</i>					0.42	
fi43	-31	-39	-5.4	+6.6	366.1	x	x	x	x	x		0.41
fi44	-34	-39	-6.9	+5.5	376.7	<i>no Raman analyses</i>					0.44	
fi64		-38		+4.0	389.5	8000	15439	27181	1510	597		0.62
fi23	-31.9		-2.4	+7.2	313.6	-	-	299272	6248	1532	H ₂ S at 2578 other gases at 2951, 3014, 3065	0.33
fi45	-32	-46	-4.0	+3.7	317.0	<i>no Raman analyses</i>					0.24	
fi29	-35		-5.6	-0.8	282.0	<i>no Raman analyses</i>					0.21	

red = strong fluorescence

green = transition type of fluid inclusions

* corrected for atmospheric N₂

x = present, but not quantified

Sample 67E, Type 3 Fluid Inclusions Quartz

	Microthermometry			Area Raman Peaks		Volume
	T_n in °C	T_m (ice) in °C	T_h (LV→L) in °C	CH ₄ 2914 cm ⁻¹	H ₂ 4152 cm ⁻¹	area fraction (vap)
fi2	-30.4	-0.5	207.7	2087	448	0.14
fi10	-41	-1.0	271.2	4735	2121	0.19
fi11	-28	-0.8	288.8	<i>no Raman analyses</i>		0.23
fi12		-0.7	316.7	1337	3156	0.27
fi14	-37	-0.5	192.0	876	1600	0.11
fi15	-40	-0.6	242.9	809	1368	0.20
fi16	-30	-0.4	187.0	1158	1914	0.34 neck.
fi18	-29.5	-1.0	281.2	<i>no Raman analyses</i>		0.32
fi20	-28	-1.0	277.7	<i>no Raman analyses</i>		0.19
fi24	-29	-0.1	232.0	<i>no Raman analyses</i>		0.27
fi25	-29	+1.0	decrep.	<i>no Raman analyses</i>		0.10
fi26	-31	-0.4	189.0	<i>no Raman analyses</i>		0.13
fi27	-39	-0.3	decrep.	436	1001	0.16
fi28	-38.5	-0.9	291.4	<i>no Raman analyses</i>		0.20
fi30	-35	-0.9	221.0	<i>no Raman analyses</i>		0.08 irreg.
fi31	-35	-0.6	234.0	<i>no Raman analyses</i>		0.17
fi32	-31	-0.5	232.2	<i>no Raman analyses</i>		0.16
fi33	-37	-0.3	188.9	<i>no Raman analyses</i>		0.10
fi36	-38	-0.4	194.8	<i>no Raman analyses</i>		0.15
fi40	-35	-0.3	239.1	<i>no Raman analyses</i>		0.20
fi42	-37	-0.8	262.7	2449	1506	0.15
fi46	-40	-0.4	202.0	<i>no Raman analyses</i>		0.21
fi47	-39	-0.0	149.3	<i>no Raman analyses</i>		0.10
fi48	-34	-0.5	247.3	<i>no Raman analyses</i>		0.14
fi49	-40	-0.2	126.8	<i>no Raman analyses</i>		0.08
fi50	-38	-0.2	131.4	<i>no Raman analyses</i>		0.05
fi51	-39	-0.4	184.5	<i>no Raman analyses</i>		0.18
fi52	-35	-2.6	313.3	<i>no Raman analyses</i>		0.31
fi53	-36.8	-0.7	277.2	<i>no Raman analyses</i>		0.23
fi54	-35	-0.4	201.0	<i>no Raman analyses</i>		0.17
fi55	-39	+0.1	146.8	<i>no Raman analyses</i>		0.10
fi56	-37	-0.8	142.7	<i>no Raman analyses</i>		0.10
fi57	-36	-0.3	151.4	2055	3024	0.11
fi58	-37	-0.6	214.6	1781	3040	0.13
fi59	-31	-0.4	197.0	<i>no Raman analyses</i>		0.25
fi60	-39	-0.5	212.2	<i>no Raman analyses</i>		0.17
fi61	-39	-1.8	decrep.	<i>no Raman analyses</i>		0.09
fi62	-40	-0.7	232.5	6500	3822	0.22
fi63	-39	-0.3	187.6	x	1738	0.14
fi68			200.4	<i>no Raman analyses</i>		
fi69			189.5	<i>no Raman analyses</i>		
fi70			196.3	<i>no Raman analyses</i>		
fi71			219.0	<i>no Raman analyses</i>		
fi72			187.6	<i>no Raman analyses</i>		0.17
fi73			189.6	<i>no Raman analyses</i>		
fi74			194.0	<i>no Raman analyses</i>		
fi75			195.0	<i>no Raman analyses</i>		

red = strong fluorescence

x = present, but not quantified

Sample 85A, Fluid Inclusions in Tourmaline

85A Tourm	Microthermometry			Area Raman Peaks			Volume	minerals
	T _m (ice) in °C	T _m (sas) in °C	T _h (LV→L) in °C	CO ₂ 1283 cm ⁻¹	CO ₂ 1385 cm ⁻¹	CH ₄ 2914 cm ⁻¹	area (vap) fraction	
fi1	-7.7	+22.3	374.3				0.45	b
fi2	-7.1	+20.8	359.8	921	1128	3266	0.43	B
fi3	-7.9	+16.4	376.4				0.37	B
fi4	-7.4	+17.6	d	1117	1803	1937		B
fi5	-7.5	+15.8	381.8				0.44	
fi6	-7.2	+18.3	381.3	x	x	?	0.45	B, As ₄ O ₆
fi7	-9.0	+24.9	379.8					B, As ₄ O ₆
fi8	-6.6		377.0					
fi9	-5.1	+15.4	374.9	x	x	?	0.35	
fi10	-7.6		376.4		x		0.35	
fi11	-7.1	+25.7	378.8				0.48	B
fi12	-7.2		377.6				0.40	B, As ₄ O ₆
fi13	-4.7		216.3				0.13 (neck)	
fi14	-7.2		250.9				0.22 (neck)	
fi15	-7.1	+8.6	378.2				0.42	B
fi16	-7.0	+22.0	377.4				0.44	B
fi17	-6.9	+17.0	376.1				0.48	B
fi18	-6.6		376.7				0.46	
fi19	-7.0		377.8	x	x	?	0.39	
fi20	-8.1	+4.3	356.7					
fi21	-9.3		375.1	13989	23194	?	0.40	B
fi22	-8.1		375.0	1068	2019	?	0.41	
fi23	-6.2		378.2				0.49	
fi24	-6.5		286.0				0.28	
fi25	-1.3		363.6	3950	6749	?	0.42	B, As
fi26	-6.4	+25.8	379.1				0.42	B
fi27	-6.5	+23.6	375.5	515	982	655	0.37	B
fi28	-6.2		378.6	x	x	?	0.43	B
fi29	-6.0		378.7	1299	2089	?	0.47	b
fi30	-6.3	+25.3	379.9	2250	2794	562	0.41	B
fi31	-5.9		369.8				0.30	
fi32	-6.1		369.9				0.31	
fi33	-6.5		370.9				0.38	
fi34	-5.1		370.4				0.45	
fi35	-5.4		375.6				0.40	
fi36	-2.8		359.8	2438	3937	?	0.55	
fi37	-5.0		370.5				0.31	
fi38	-9.3		373.4	3204	5665	?	0.44	
fi39	-0.2		362.5	5653	10400	?	0.44	
fi40	-0.4		365.9	17133	27179	928	0.44	
fi41	0.2		361.5	23479	36838	1108	0.44	

red = strong fluorescence

B = sassolite crystal

b = dissolved sassolite

As = arsenic

As₄O₆ = arsenolite

x = trace, not quantified

Sample 85A, Fluid Inclusions in Tourmaline

85A Tourmaline		Raman Analyses (numbers are peak area's)							
		CO ₂ 1286 cm ⁻¹	CO ₂ 1388 cm ⁻¹	CH ₄ 2917 cm ⁻¹	H ₂ S	N ₂	H ₂	int.	solids
TUR A	fia	683	1364	2400				w	B
	fib	416	720	270				ww	B
	fic	2173	3350	480		x		w	B
	fid	2680	4130	740		x		w	B
	fie	1167	2350	906		x		w	As
	fif	4485	7750	11956			740		
TUR B	fig		x	924				w	
	fih			x				ww	
	fii	8816	13580	2870		608			b
	fij		x	66620					
	fik	560	940	44703	x	1800			
	fil	5470	11190	1000					b
	fim	6250	10500	14328	x	x			
	fin	3840	5213	23719	1585	1830			b
	fio	3150	5190	18572					
TUR C	fip	4784	7716	x	x				
	fiq	6222	13000	850	2115				
	fir	10440	17727	4159	2980				
	fis	44115	65363	2800					
	fit	24057	40366	2876	x				
	fiu	14921	23075	840					
	fiv	2027	3200	5421					B
	fiw	13593	19952	11100		x			
	fix			2922				w	
	fiy	3282	5375	6405		590			
	fiz	2088	5500	trace					B

int. = relative intensity of Raman spectrum

solids = entrapped solid phases

w = weak

ww = very weak

B = sassolite crystal

b = dissolved sassolite

As = arsenic

x = trace, not quantified

Sample 85A, Fluid Inclusions in Quartz

85A Qtz1	Microthermometry			Area Raman Peaks			Volume
	T _n in °C	T _m (ice) in °C	T _n (LV→L) in °C	CO ₂ 1283 cm ⁻¹	CO ₂ 1385 cm ⁻¹	CH ₄ 2914 cm ⁻¹	area (vap) fraction
fi1	-32.8	-2.6	227.0				0.22
fi2	-36.8	-3.8	220.1				0.13
fi3	-38.1	-3.9	239.0				0.22
fi4	-37.6	-4.2	238.0	3088	6258*	x	0.19
fi5	-33.1	-2.7	236.2	?	250	2184	0.24
fi6	-37.2	-4.1	236.3			x	0.18
fi7	-33.5	-3.4	227.1				0.12
fi8	-37.0	-2.5	241.6	2469	5301*	804	0.24
fi9	-35.5	-4.0	211.7	6017	9281	1447	0.18
fi10	-32.1	-0.6	221.2	x	x	2142	irreg
fi11	-30.9	-2.4	227.7	1775	2959*	3473	0.18
fi12	-29.0	-0.7	227.5				0.13
fi13	-34.2	-0.6	191.2				0.19
fi14	-32.3	-4.4	252.0				0.24
fi15	-34.9	-3.6	247.2				irreg
fi16	-34.6	-2.9	235.4	768	1507*	x	0.18
fi17	-31.7	-0.4	222.9	x	x	370	0.20
fi18	-31.7	-0.6	d				irreg
fi19	-40.5	-3.9	241.3	6233	9545	3942	0.18
fi20	-37.7	-4.3	204.3	4740	7000*	2132	0.16
fi21	-41.8	-3.2	245.1	1157	2700*	1006	0.17
fi22	-38.2	-3.4	235.8	3157	6297*	1182	0.20
fi23	-34.0	-3.1	248.0	3478	6100*	611	0.29
fi24	-38.0	-3.6	257.3	5721	9980	3695	0.18
fi25	-31.9	-3.7	239.4	5479	7130	2061	irreg
fi26	-33.5	-3.4	d				-
fi27	-37.6	-2.7	228.7	360	621	899	0.17
fi28	-38.8	-2.3	228.4	?	?	1270	0.20
fi29	-33.0	-1.5	204.1	870	1372	1138	0.16
fi30	-32.8	-1.3	232.9	599	950*	482	0.28
fi31				4017	6958	544	
fi32				1397	2595	1095	
fi33							
fi34				x	x	x	
fi35				x	x		
fi36				x	x		

red = strong fluorescence

* = interference with minor peak at 1379 cm⁻¹

d = decrepitated

x = present but not quantified

Sample 85A, Fluid Inclusions in Quartz

85A Qtz2	Microthermometry			Area Raman Peaks			Volume
	T _n in °C	T _m (ice) in °C	T _h (LV→L) in °C	CO ₂ 1283 cm ⁻¹	CO ₂ 1385 cm ⁻¹	CH ₄ 2914 cm ⁻¹	area (vap) fraction
fi1	-31.9	-2.8	243.6	1937	3175	3218	0.15 (ir) + mica
fi2	-32.8	-2.7	245.1				0.19
fi3	-31.9	-2.8	201.4	1720	4050	4264	0.15 (ir)
fi4	-32.9	-2.9	239.3	2066	4409*	2829	0.17
fi5	-32.4	-2.7	239.6	6830	11212*	9336	irreg
fi6	-33.9	-3.1	247.2	5125	8246	8010	0.20
fi7	-32.4	-2.9	238.3	3258	4950	3700	0.20
fi8	-32.5	-2.7	237.5	5426	9606*	6567	0.17 + mica
fi9	-32.6	-3.0	269.4	22230	35613	19830	0.20
fi10	-32.7	-2.5	245.1				0.18 + mica
fi11	-	-	-	7637	11111	2735	irreg
fi12	-36.4	-3.2	287.8	15866	28238	6944	0.21
fi13	-31.9	-2.7	254.3	6570	9500*	25863	0.20
fi14							0.27 + mica
fi15							irreg
fi16	-29.9	-2.6	247.1	5181	9568*	5092	0.17
fi17			d				0.14
fi18				11510	17280	2200	0.20
fi19	-34.5	-4.1	d				0.10
fi20	-34.5	-3.0	d				0.15
fi21	-34.3	-3.0	212.8	2250	4200*	750	0.17
fi22	-34.5	-3.0	d				0.17
fi23	-33.9	-2.7	198.7				0.22
fi24	-32.9	-2.8	208.9	1205	2614*	360	0.19
fi25	-34.6	-3.1	d				0.18
fi26	-37.8	-3.0	215.4	4448	8000*	1483	0.14
fi27	-33.9	-2.7	207.8	2118	3565	1468	0.16 + mica
fi28	-34.5	-2.2	205.7	x	468	304	0.12
fi29	-33.7	-3.1	207.8				0.14
fi30	-33.8	-3.1	217.4	1901	3825	770	0.16
fi31	-35.2	-3.2	235.0				0.21
fi32	-36.6	-3.4	199.0	1306	3590	1116	0.19
fi33	-35.9	-3.3	217.4	8983	19825*	4698	
fi34	-31.9	-2.7	235.7				0.21
fi35	-32.4	-2.7	243.3	3151	5552	3405	irreg
fi36	-32.9	-3.0	241.3				0.17
fi37	-43.9	-2.8	218.4				0.14
fi38	-33.9	-2.8	238.7	2382	3487	2658	0.16
fi39	-35.9	-2.5	235.6				irreg
fi40	-44.9	-2.9	230.2	10170	16030*	6958	0.17

red = strong fluorescence

* = interference with minor peak at 1379 cm⁻¹

d = decrepitated

x = present but not quantified

H₂O-NaCl-H₃BO₃ system*Invariable points*

Eutectic binary H ₂ O-H ₃ BO ₃ :	-0.76 °C, 2.5 mass% H ₃ BO ₃
Eutectic binary H ₂ O-NaCl:	-21.2 °C, 23.73 mass% NaCl
Peritectic binary H ₂ O-NaCl:	+0.1 °C, 26.24 mass% NaCl
Eutectic ternary H ₂ O-NaCl-H ₃ BO ₃	-21.4 °C, 23.02 mass% NaCl, 1.46 mass% H ₃ BO ₃
Peritectic ternary H ₂ O-NaCl-H ₃ BO ₃	0.0 °C, 25.7 mass% NaCl, 2.09 mass% H ₃ BO ₃

Definition of cotectic lines:

general parameters: $T_x = T_c + 21.4$

$$ratio = \frac{w(NaCl)}{w(H_3BO_3)}$$

Ice + Sassolite cotectic

$$w(H_2O) = 75.52 + 0.58847 \cdot T_x + 0.0058476 \cdot (T_x)^2 + 0.00080962 \cdot (T_x)^3$$

$$ratio = 15.767 - 1.0621 \cdot T_x + 0.032717 \cdot (T_x)^2 - 0.0008782 \cdot (T_x)^3$$

Ice + Hydrohalite cotectic

$$w(H_2O) = 75.52 + 6.6 \cdot T_x$$

$$w(NaCl) = 23.02 + 0.7 \cdot T_x$$

sum of fractions: $w(H_3BO_3) + w(NaCl) + w(H_2O) = 1$

Hydrohalite + Sassolite cotectic

$$w(H_2O) = 75.52 - 0.12778 \cdot T_x + 0.0012568 \cdot (T_x)^2$$

$$ratio = 15.767 - 0.015444 \cdot T_x - 0.0068564 \cdot (T_x)^2$$

Hydrohalite + Halite cotectic

$$w(H_2O) = 72.21 + 15.5 \cdot T_C$$

$$w(NaCl) = 25.70 + 5.4 \cdot T_C$$

$$\text{sum of fractions: } w(H_3BO_3) + w(NaCl) + w(H_2O) = 1$$

Halite + Sassolite cotectic

$$w(H_2O) = 72.21 - 0.058816 \cdot T_C - 0.00051637 \cdot (T_C)^2 - 6.8466 \cdot 10^{-6} \cdot (T_C)^3$$

$$\frac{1}{\text{ratio}} = 0.081323 + 0.0029855 \cdot T_C + 4.8861 \cdot 10^{-6} \cdot (T_C)^2 + 5.7522 \cdot 10^{-7} \cdot (T_C)^3$$

Isotherms in the sassolite-field

$$10 \text{ }^\circ\text{C: } w(H_3BO_3) = 3.5277 - 0.026559 \cdot w(NaCl) + 8.7468 \cdot 10^{-7} \cdot w(NaCl)^2$$

$$30 \text{ }^\circ\text{C: } w(H_3BO_3) = 6.3406 - 0.10183 \cdot w(NaCl) + 0.001679 \cdot w(NaCl)^2$$

$$50 \text{ }^\circ\text{C } w(H_3BO_3) = 10.237 - 0.14858 \cdot w(NaCl) + 0.002154 \cdot w(NaCl)^2$$

$$70 \text{ }^\circ\text{C } w(H_3BO_3) = 15.768 - 0.23276 \cdot w(NaCl) + 0.0039404 \cdot w(NaCl)^2$$

$$90 \text{ }^\circ\text{C } w(H_3BO_3) = 23.276 - 0.34718 \cdot w(NaCl) + 0.0068058 \cdot w(NaCl)^2$$